# Importance of anisotropic Coulomb interaction in LaMnO_{3}

Thomas A. Mellan, Furio Corà, Ricardo Grau-Crespo, and Sohrab Ismail-Beigi

# The importance of anisotropic Coulomb interaction in LaMnO$_3$

Thomas A. Mellan,[1] Furio Cora,[1] Ricardo Grau-Crespo,[2] and Sohrab Ismail-Beigi[3, 4]

$^1$*Department of Chemistry, University College London,*
*20 Gordon Street, London WC1H 0AJ, United Kingdom*
$^2$*Department of Chemistry, University of Reading,*
*Whiteknights, Reading RG6 6AD, United Kingdom*
$^3$*Department of Applied Physics, Yale University, New Haven, Connecticut, USA*
$^4$*Center for Research on Interface Structures and Phenomena (CRISP), Yale University, New Haven, Connecticut, USA*

In low-temperature anti-ferromagnetic LaMnO$_3$, strong and localized electronic interactions among Mn $3d$ electrons prevent a satisfactory description from standard local density and generalized gradient approximations in density functional theory calculations. Here we show that the strong on-site electronic interactions are described well only by using direct *and* exchange corrections to the intra-orbital Coulomb potential. Only DFT$+U$ calculations with explicit exchange corrections produce a balanced picture of electronic, magnetic and structural observables in agreement with experiment. To understand the reason, a rewriting of the functional form of the $+U$ corrections is presented that leads to a more physical and transparent understanding of the effect of these correction terms. The approach highlights the importance of Hund's coupling (intra-orbital exchange) in providing anisotropy across the occupation and energy eigenvalues of the Mn $d$ states. This intra-orbital exchange is the key to fully activating the Jahn-Teller distortion, reproducing the experimental band gap and stabilizing the correct magnetic ground state in LaMnO$_3$. The best parameter values for LaMnO$_3$ within the DFT (PBEsol) $+U$ framework are determined to be $U = 8$ eV and $J = 1.9$ eV.

PACS numbers: 71.15.Mb, 71.20.-b, 75.30.Et, 75.25.Dk

## I. INTRODUCTION

LaMnO$_3$ (LMO) is characteristic of the ABO$_3$ family of strongly correlated transition metal oxide perovskites, which generally exhibit complex phase diagrams, as a result of subtle coupling across several distinct mechanisms.[1] Bulk, thin film, and interfacial LaMnO$_3$ are subject to a multitude of symmetry breaking mechanisms, including crystal field,[1] octahedral distortion,[2] orbital ordering and Jahn-Teller distortion,[3–6] Mott-type strong $d$ electron Coulomb interactions (direct and exchange),[7,8] and charge transfer ordered (Verwey) states[9–11]. All of these mechanisms are believed to exist and compete in varying ways in this material. As a result, LaMnO$_3$ naturally exhibits a rich phase diagram as a function of temperature and pressure[6] as well as dopant concentration,[12,13] which together make LaMnO$_3$ the single most examined metal oxide in the LaXO$_3$ class (where X is a transition metal atom).[14] Doping on the ABO$_3$ A site provides a particularly rich field of experimentally observed phenomena, with both Na and Ca doped La$_{1−x}$A$_x$MnO$_3$ exhibiting colossal magneto resistance (CMR)[15,16] and a Seebeck coefficient that can exhibit positive or negative values which may lead to potential thermopower applications.[17] Pure bulk LaMnO$_3$ is spin polarized and non-polar, but recent theoretical work shows that the magnetic state in Sr doped La$_{1−x}$Sr$_x$MnO$_3$ may be controlled through variation in the electric polarization state.[13] Recent multi-ferroic theory predicts novel magnetic properties due to $t_{2g}$ ferromagnetic superexchange in Ti doped LMO interfaces.[18] Finally, the interface between La$_{1−x}$Sr$_x$MnO$_3$ and a fer-

roelectric shows a polar state that also has a reversible orbital polarization.[19]

This interest in LMO from condensed matter and materials scientists underscores the value of a reliable first principles description based on, for example, density functional theory (DFT). In particular the magnetic, electronic and crystal structure should be accessible simultaneously within a low-cost computational framework. Unfortunately previous Hartree-Fock, DFT and hybrid-functional examinations of bulk LMO show that that obtaining a satisfactory description is not trivial.[1,20]

In this work we show the limitations and successes of two different DFT$+U$ methods. The Dudarev *et al.* Coulomb correction,[21] here called $U_{\text{eff}}$, averages out exchange effects of the Mn $d$ shell, and we show that it cannot simultaneously reproduce the bulk band gap, structure and magnetism. The dedicated anisotropic exchange term in the Liechtenstein *et al.* Coulomb correction,[22] here called $U|J$, dramatically improves the description of LMO. The $U|J$ method answers the specific call for a practical DFT-based methodology capable of reproducing the gap, structure and magnetism simultaneously in LMO.[23] This is useful as understanding the coupling between electronic, magnetic and lattice degrees of freedom in LMO is a matter of persistent interest.[2,23,24]

Using the $U|J$ method we show the importance of Hund's coupling in LMO. Intra-orbital exchange can energetically order the orbitals of the Mn $t_{2g}{}^3 e_g{}^1$ ion, which in turn strongly affects *inter-orbital* magnetism and the size of the LMO band gap. The Mn $e_g{}^1$ occupancy polarization[19,25]

$$\pi^{e_g\sigma} = \frac{f_{x^2-y^2\sigma} - f_{3z^2-r^2\sigma}}{f_{x^2-y^2\sigma} + f_{3z^2-r^2\sigma}}, \qquad (1)$$

for the $x^2 - y^2$ and $3z^2 - r^2$ occupancy eigenvalues ($f$) where $\sigma$ labels spin, is highly sensitive to intra-orbital exchange term $J$ in the $U|J$ scheme. By modifying the sign and value of $\pi^{e_g\sigma}$, we correct the DFT description of Jahn-Teller (JT) distortion, and the electronic and magnetic structures of LMO. In addition the $U|J$ calculations provide insight into the origin of magnetic, electronic and structural ordering in LMO.

## II. METHODOLOGY

Periodic plane wave density functional theory (DFT) calculations are performed using the VASP software,[26,27] the local density approximation (LDA PZ81)Perdew and Zunger [28], and the generalized gradient approximation (GGA) in the form of the Perdew-Burke-Erzenhof solids-adapted exchange correlation functional (PBEsol).[29,30] Valence electrons are described using the projector augmented wave (PAW) method[31,32] with core states (up to $4d$ in La, $2p$ in Mn, and $2s$ in O) frozen at their atomic reference states. Plane-waves were cutoff above a kinetic energy of 520 eV, and a $5\times4\times5$ **k**-point mesh of was employed for the LaMnO$_3$ unit cells. All relaxed structures fulfill a convergence criterion of less than 0.01 eV/Å, for both ionic forces and volume-normalized stresses (as standard in VASP).

DFT has known shortcomings in the prediction of the electronic structure of materials with localized electronic states.[22,33,34] A typical example are the bands derived from Mn $d$ orbitals in LaMnO$_3$: the errors can be corrected to various extents by employing Hubbard-U type corrections to account for intra-atomic Coulomb interactions in the DFT+$U$ approach.[21,22,34] The most popular and simplest Coulomb correction is the "Spherically Averaged" scheme of Dudarev *et al.*,[21] here called DFT+$U_{\text{eff}}$, which has only a single effective $U$ parameter, $U_{\text{eff}}$. A more sophisticated approach is the "Rotationally Invariant" scheme of Lichtenstein and Zaanen,[22] which we label here as DFT+$U|J$. Note the simpler Dudarev $U_{\text{eff}}$ approach was developed after the Liechtenstein $U|J$ approach, and both are fully rotationally invariant.

Both DFT+$U$ methodologies add Hartree-Fock type corrections to the DFT total energy that act on a local sub-space of atomic-like orbitals. The DFT+$U_{\text{eff}}$ total energy is given by

$$E_{\text{DFT}+U_{\text{eff}}} = E_{\text{DFT}} + \frac{U_{\text{eff}}}{2} \sum_{at} \sum_{i,\sigma} (f_{i\sigma} - f_{i\sigma}^2) \qquad (2)$$

where $E_{\text{DFT}}$ refers to some chosen flavor of electron density-based exchange-correlation approximation (LDA or GGA in our work). The index $at$ specifies the Mn sites where the correction is performed. The eigen-occupations $f_{i\sigma}$ of the electronic on-site density matrix are labeled by spin $\sigma$ and index $i$ which represents a linear combination of angular momentum quantum numbers (which in our case ranges over the five magnetic quantum numbers $m = -2, -1, 0, 1, 2$ for the $3d$ Mn orbitals). $U_{\text{eff}} = U - J$ is the Hubbard-type energy parameter for this approach while $U$ and $J$ are the separate direct and exchange Coulomb parameters[22] (see also Appendix A).

For our work here, the DFT+$U|J$ total energy is best rewritten as an added correction to the DFT+$U_{\text{eff}}$ approach (as detailed in Appendix A) given by

$$E_{\text{DFT}+U|J} = E_{\text{DFT}} + E_{\text{corr}}$$
$$= E_{\text{DFT}} + \frac{U_{\text{eff}}}{2} \sum_{at} \sum_{i,\sigma} (f_{i\sigma} - f_{i\sigma}^2) +$$
$$\frac{1}{2} \sum_{\sigma\sigma',ij} \text{C}_{ij}^{\sigma\sigma'} f_{i\sigma} f_{j\sigma'} - \Delta\text{X}_{ij}^{\sigma} f_{i\sigma} f_{j\sigma} \delta_{\sigma\sigma'}. \quad (3)$$

The correction to the DFT band energy eigenvalue $\epsilon_{i\sigma}$ stems from the occupancy derivative of the correction terms given by

$$\Delta\epsilon_{i\sigma}^{\text{corr}} = \frac{\partial E_{\text{corr}}}{\partial f_{i\sigma}} = U_{\text{eff}} \left( \frac{1}{2} - f_{i\sigma} \right)$$
$$+ \sum_{j,\sigma'} \text{C}_{ij}^{\sigma\sigma'} f_{j\sigma'} - \Delta\text{X}_{ij}^{\sigma} f_{j\sigma} \delta_{\sigma\sigma'},$$

where the first term is the $U_{\text{eff}}$ correction and the second and third terms are the added contribution from the $U|J$ scheme. For compactness and for use below, it is useful to collect all occupancies or energy eigenvalues for the same spin into a vector $f_\sigma$ or $\epsilon_\sigma$ in order write these corrections in matrix notation. For atomic $d$ shells, the Appendix A shows that

$$\Delta\epsilon_\sigma^{\text{corr}} = U_{\text{eff}} \left( \frac{1}{2} - f_\sigma \right) + J\text{A}^\sigma f_\sigma + J\text{B}^\sigma f_{\bar{\sigma}} \qquad (4)$$

where $\bar{\sigma}$ represents the opposite spin to $\sigma$. For canonical $t_{2g}$ and $e_g$ orbitals, the dimensionless matrices $\text{A}^\sigma$ and $\text{B}^\sigma$ are

$$\text{A}^\sigma = \begin{pmatrix} & 3z^2-r^2 & x^2-y^2 & xy & yz & xz \\ \hline 3z^2-r^2 & 0 & -0.52 & -0.52 & 0.52 & 0.52 \\ x^2-y^2 & -0.52 & 0 & 0.86 & -0.17 & -0.17 \\ xy & -0.52 & 0.86 & 0 & -0.17 & -0.17 \\ yz & 0.52 & -0.17 & -0.17 & 0 & -0.17 \\ xz & 0.52 & -0.17 & -0.17 & -0.17 & 0 \end{pmatrix}$$

and

$$\text{B}^\sigma = \begin{pmatrix} & 3z^2-r^2 & x^2-y^2 & xy & yz & xz \\ \hline 3z^2-r^2 & 1.14 & -0.63 & -0.63 & 0.06 & 0.06 \\ x^2-y^2 & -0.63 & 1.14 & 0.29 & -0.40 & -0.40 \\ xy & -0.63 & 0.29 & 1.14 & -0.40 & -0.40 \\ yz & 0.06 & -0.40 & -0.40 & 1.14 & -0.40 \\ xz & 0.06 & -0.40 & -0.40 & -0.40 & 1.14 \end{pmatrix}.$$

Both DFT+$U$ methodologies permit the description of electron localisation phenomena, that stem from Hartree-Fock physics and the related removal of self-interaction errors, which enable essential long-range ordering (orbital, spin, charge and lattice degrees of freedom).[33] For Mn in LMO, delocalised $s$ and $p$ orbitals typify the weakly correlated electronic states successfully described by DFT, while the localised Mn $d$ states require the $+U$ correction. In the DFT+$U_{eff}$ approach, $U_{eff}$ in Equation (2) provides occupation-dependent corrections to DFT, while the DFT+$U|J$ approach in Equation (3) adds further degrees of explicit spatial/orbital dependent corrections. Both corrections provide a basis for for energy splitting of $d$ orbitals (and related symmetry breaking and orbital polarization) on top of splittings due to spin exchange and/or crystalline geometrical distortions already present at the LDA or GGA density functional level.

The $U|J$ correction variety in Equation (4) is most relevant to materials with strongly interacting electrons with an explicit orbital symmetry dependence,[35] for example, Fe-based superconductors,[36] heavy fermion metals,[37] non-collinear magnetic materials,[38,39] and orbitally ordered materials in which Hund's coupling is critical to establishing the correct insulating or metallic character.[40] Although the anisotropic exchange corrections to DFT have successfully been used to describe manganese oxides in the past,[39,41,42] we believe our work is the first explicit calculation and analysis of the $U|J$ exchange matrix elements and anisotropic splitting for LaMnO$_3$.

In our work, our global coordinate system is chosen to align the orthogonal $x', y,' z'$ axes along the LMO unit cell $(a, b, c)$ vectors. A local $x, y, z$ basis for each Mn is defined by aligning the local axes with the Mn-O bonds of each tilted MnO$_6$ octahedron (see Figures 1 and 4): the local $x$ axis is chosen along the shortest Mn-O bond (strongly JT active), the local $y$ axis along the intermediate length Mn-O bond (here called apical), and the local $z$ axis is along the longest Mn-O bond (strongly JT active). Use of this local basis is more convenient for analysis of the electronic states and occupancies. The transformation from global to local coordinates is performed for each relaxed geometry by employing a direct polynomial-based transformation of orbitals (detailed in Appendix B). Unless specifically noted, orbitals and occupancies refer to the local basis.

### III. RESULTS AND DISCUSSION

At 750 K LaMnO$_3$ (LMO) undergoes a structural phase transition, transforming from cubic to orthorhombic symmetry. Under ambient conditions the orthorhombic perovskite has a paramagnetic spin structure. Below the Néel temperature of $T_N \approx 140$ K,[43] LMO is an insulator with A-type antiferromagnetic (A-AFM) spin ordering. In the low $T$ orthorhombic P$nma$ LMO shown in Figure 1, experimental reports of lattice parameters are
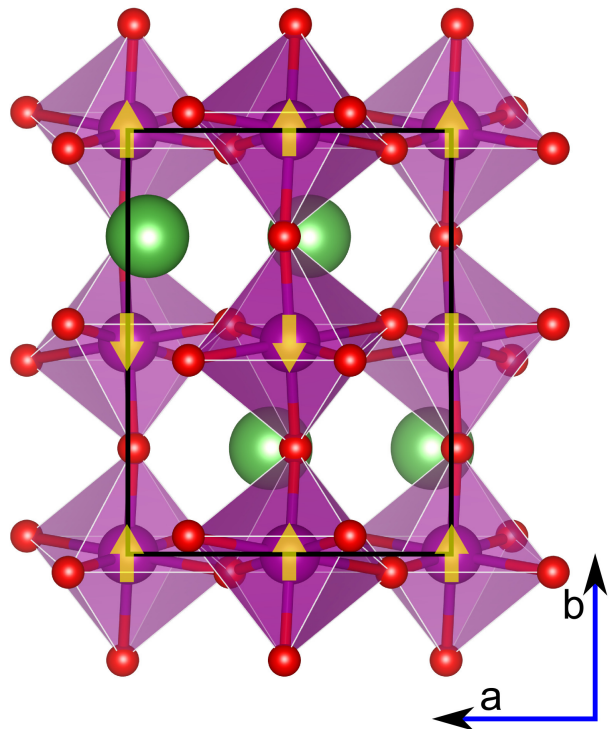


Figure 1: (001) face of A-type antiferromagnetic (A-AFM) LaMnO$_3$ . Mn in purple, La in green and O in red. Arrows indicate direction of spin polarization on Mn ions.

$a = 5.736$ Å, $b = 7.703$ Å and $c = 5.540$ Å by neutron powder diffraction[44]. To support the A-AFM ordering in LaMnO$_3$, the Mn $d^4$ electrons exchange anisotropically: ferromagnetic (FM) coupling exists between Mn in {010} planes while AFM coupling exists between successive planes along [010].

The reported experimental band gaps in LMO cover a range of values, depending on whether the gap is determined from measurements on conductivity (0.24 eV),[17] optical absorption (1.1 eV),[45] photoemission (1.7 eV),[46] optical conductivity (1.9 eV),[47] or resonant Raman spectroscopy (2 eV).[48] DFT is a single-particle theory, so even with the exact exchange-correlation functional, it can only describe the fundamental (quasiparticle) band gap and not the optical one. We therefore consider the most appropriate reference value to be the 1.7 eV photoemission gap measured by Saitoh et al.[46]. We note that recent computational work by Lee et al.[49] predicts a direct gap of 1.1 eV, in agreement with the optical absorption gap of 1.1 eV measured by Arima et al.[45]. The value of the optical gap is generally lower than the fundamental gap due to electron-hole interactions (i.e., excitonic effects). Such two-particle interactions are not included in standard one-particle DFT, so we believe the most reliable comparisons should be made between a benchmark indirect experimental photoemission gap such as the 1.7 eV Saitoh gap[46] and the indirect DFT gap.

One of our main practical considerations here is to reproduce the different facets of the above experimental

Table I: LDA+$U_{\text{eff}}$ and GGA+$U_{\text{eff}}$ results for the energy gap $E^{\text{Gap}}$ (in eV), for the A-AFM and FM phases, and the total energy difference $\Delta E = E^{\text{A-AFM}} - E^{\text{FM}}$ (in meV) per formula unit of LaMnO$_3$. The crystal structure is held fixed at the experimental geometry.

| $U_{\text{eff}}$ (eV) | LDA (PZ81) | | | GGA (PBEsol) | | |
|---|---|---|---|---|---|---|
| | $E^{\text{Gap}}_{\text{A-AFM}}$ | $\Delta^{\text{Gap}}_{\text{FM}}$ | $\Delta E$ | $E^{\text{Gap}}_{A-\text{AFM}}$ | $\Delta^{\text{Gap}}_{\text{FM}}$ | $\Delta E$ |
| 0 | 0.0 | 0.0 | -22 | 0.2 | 0.0 | -13 |
| 2 | 0.5 | 0.0 | -5 | 0.6 | 0.0 | 1 |
| 4 | 1.0 | 0.0 | 4 | 1.0 | 0.0 | 8 |
| 6 | 1.3 | 0.1 | 10 | 1.3 | 0.1 | 14 |
| 8 | 1.4 | 0.2 | 14 | 1.4 | 0.2 | 17 |

description. To do this, DFT calculations are performed screening through different levels of Coulombic localisation.

### A. Description of LaMnO₃ using DFT+$U$

Previous work has applied the single term $U_{\text{eff}}$ approach to calculations on bulk LaMnO$_3$.[1,13,23,50] The failure of this approach to *simultaneously* describe the energy gap, structure and magnetism drives us to systematically examine the $U_{\text{eff}}$ method. These initial results also provide context for the more sophisticated $U|J$ method and analysis of its merits and behaviour below.

#### 1. Experimental LaMnO₃ structure *via* DFT+$U_{\text{eff}}$

Standard LDA (PZ81) and GGA (PBEsol) with $U_{\text{eff}} = 0$ eV both successfully stabilize the low temperature experimental A-AFM ordering as shown in Table I. However this is essentially where the success ends. As noted previously, both GGA and LDA are often unable to produce significant orbital splitting (beyond some aspects due to spin exchange and structural distortion) and also exaggerate electron delocalization due to inexact exchange (or equivalently lack of self-interaction correction). This inevitably results in a qualitatively incorrect electronic structure with a seriously underestimated band gap: both GGA and LDA with $U_{\text{eff}} = 0$ eV yield band gaps that are far too small compared to experiment.

Increasing $U_{\text{eff}}$ stabilizes the occupied $(f_{i\sigma} \gtrsim \frac{1}{2})$ eigenstates and drives orbital occupations toward binary polarization: filled states become more filled and empty states more empty. For example, increasing $U_{\text{eff}}$ from 0 to 8 eV in GGA calculations results in the following change in occupancies in the Mn $d$ manifold:

$$(f_\sigma | f_{\bar\sigma}) = \begin{pmatrix} 0.65 & 0.22 \\ 0.73 & 0.26 \\ 0.93 & 0.11 \\ 0.93 & 0.10 \\ 0.93 & 0.09 \end{pmatrix} \rightarrow \begin{pmatrix} 1.00 & 0.10 \\ 0.57 & 0.17 \\ 0.98 & 0.04 \\ 0.97 & 0.03 \\ 0.97 & 0.04 \end{pmatrix}, \quad (5)$$

where the ordering of orbitals in the local basis is
$$\begin{pmatrix} 3z^2 - r^2 \\ x^2 - y^2 \\ xy \\ yz \\ xz \end{pmatrix}.$$

The Hubbard limit of very large $U_{\text{eff}}$ typically favours FM coupling in LaMnO$_3$,[4] and Table I confirms this. The primary reason is that increasing $U_{\text{eff}}$ kills the superexchange mechanism, which scales as $\sim t^2/U_{\text{eff}}$ where $t$ is the effective Mn-Mn hopping, and this mechanism underlies the stability of A-AFM ordering in LaMnO$_3$. As a result, $e_{\text{g}}$ double-exchange is relatively strengthened and we find FM ordering. Critically, Table I shows that a large $U_{\text{eff}}$ value is required to open a satisfactory energy gap. Unfortunately this situation results in a trade-off between correct gap or correct magnetism.

#### 2. Relaxed LaMnO₃ structure *via* DFT+$U_{\text{eff}}$

When we permit the structure of LaMnO$_3$ to fully relax during the calculation, we find the results in Table II. We see that having a non-zero $U_{\text{eff}}$ improves the crystal geometry and the electronic structure description for both GGA and LDA. Particular improvements are for the large erroneous distortion in $a$ (insufficient orthorhombic character) and the opening of the band gap. Figure 2 and Table II show that the band gap increases roughly linearly with $U_{\text{eff}}$ at first but then tails off at higher $U_{\text{eff}}$. The ineffectiveness of $U_{\text{eff}}$ at high values is shown in Figure 2, and can be understood in terms of the partial $x^2 - y^2$ occupation shown in Equation (5). The partial $x^2 - y^2$ occupation damps the impact of $U_{\text{eff}}$ on the energy eigenvalue splittings since $\Delta\epsilon_{x^2-y^2\sigma} = U_{\text{eff}} \left(\frac{1}{2} - f_{x^2-y^2\sigma}\right) \approx 0$ for $f_{x^2-y^2\sigma} \approx \frac{1}{2}$. (The reason partial $e_{\text{g}}$ occupation occurs is that the $d$ manifold is not isolated but connected to the rest of the system *via* hybridization to the O $2p$ orbitals, or in other words due to the partial covalency of the Mn-O bond.)

Although adding $U_{\text{eff}}$ to GGA and LDA produces similar band gaps as per Table II, the GGA+$U_{\text{eff}}$ geometry is preferable. Overall a high value of $U_{\text{eff}} \sim 6$ eV, correcting the GGA formalism, provides on balance the best gap/structure combination. Again, an evident failure of $U_{\text{eff}}$ is its inability to predict the correct magnetic ordering at the $U_{\text{eff}}$ level required to correct the structure and the band gap.

Table II: Band gap $E^{\mathrm{Gap}}$, total energy difference $\Delta E = E^{\mathrm{A\text{-}AFM}} - E^{\mathrm{FM}}$ per unit cell, and percent errors, with respect to experiment, for lattice parameters and unit cell volume of fully relaxed A-AFM bulk LaMnO₃.

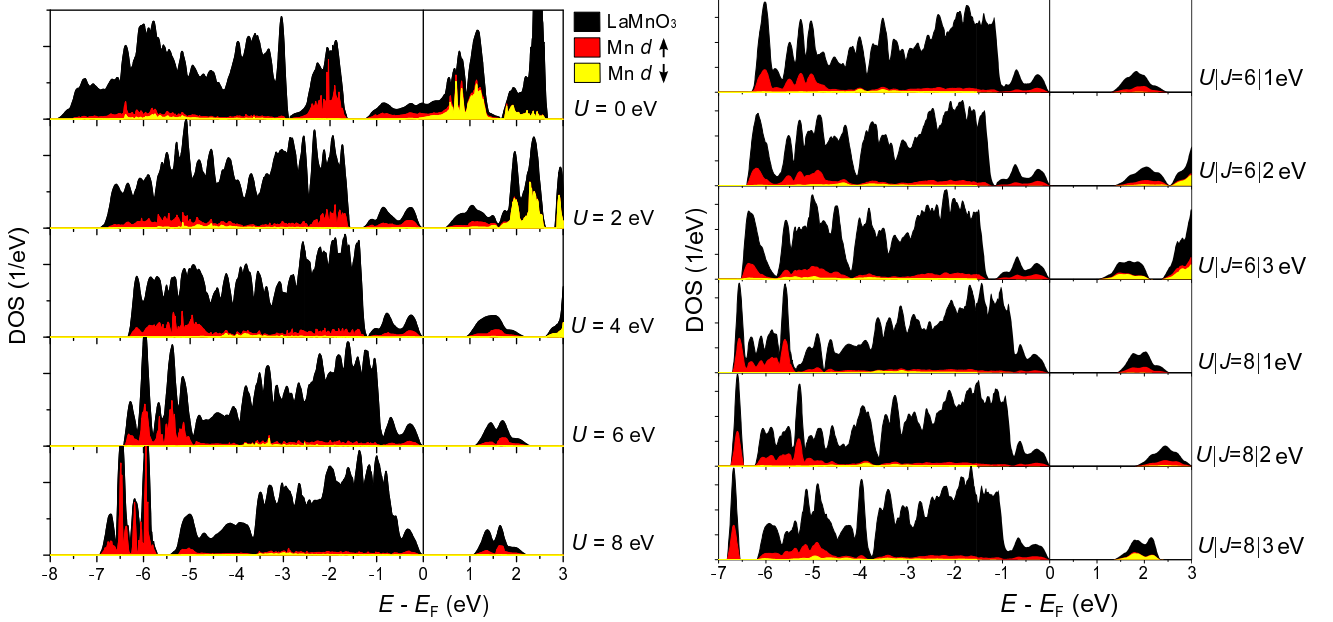| $U_{\mathrm{eff}}$ (eV) | LDA (PZ81) | | | | | | GGA (PBEsol) | | | | | |
|---|---|---|---|---|---|---|---|---|---|---|---|---|
| | $E^{\mathrm{Gap}}$ (eV) | $\Delta^{\mathrm{a}}$ (%) | $\Delta^{\mathrm{b}}$ (%) | $\Delta^{\mathrm{c}}$ (%) | $\Delta^{\mathrm{Vol.}}$ (%) | $\Delta E$ (meV) | $E^{\mathrm{Gap}}$ (eV) | $\Delta^{\mathrm{a}}$ (%) | $\Delta^{\mathrm{b}}$ (%) | $\Delta^{\mathrm{c}}$ (%) | $\Delta^{\mathrm{Vol.}}$ (%) | $\Delta E$ (meV) |
| 0 | 0.00 | -5.8 | -3.0 | -1.2 | -9.8 | 54 | 0.00 | -3.5 | -0.6 | -0.3 | -4.4 | 34 |
| 2 | 0.22 | -2.9 | -1.6 | -1.1 | -5.5 | 52 | 0.48 | -0.6 | -0.8 | -0.5 | -1.9 | 47 |
| 4 | 0.81 | -1.8 | -1.6 | -1.1 | -4.4 | 25 | 0.92 | -0.0 | -0.5 | -0.3 | -0.9 | 19 |
| 6 | 1.13 | -1.5 | -1.0 | -1.0 | -3.5 | 13 | 1.10 | 0.2 | -0.1 | -0.3 | -0.1 | 19 |
| 8 | 1.23 | -1.4 | -0.6 | -1.0 | -3.0 | 19 | 1.08 | 0.4 | 0.4 | -0.2 | 0.6 | 27 |



Figure 2: $U_{\mathrm{eff}}$ (left) and $U|J$ (right) corrected density of states for fully relaxed A-AFM LaMnO₃, as a function of energy, $E - E_{\mathrm{F}}$. Black curves show the total density of states while red and yellow curves show Mn $d$ majority spin and minority spin densities of states.

### 3. Experimental LaMnO₃ structure *via* DFT+$U|J$

Following the failure of the $U_{\mathrm{eff}}$ scheme in both single-point and relaxed geometry calculations, we turn to the DFT+$U|J$ methodology. The $U_{\mathrm{eff}}$ results conveniently suggest a reasonable starting point: since $U_{\mathrm{eff}} = U - J$, an $U|J$ correction with magnitude of approximately $U - J \approx$ 6 eV is appropriate. Results in Table III are for bulk LaMnO₃ at the experimental structure, and sample $J$ from 0 to 3 eV in conjunction with $U = 6$ eV and $U = 8$ eV. Increasing $J$ for a fixed value of $U$ stabilizes A-AFM ordering and enhances orbital splitting which further opens the band gap. Orbital splittings due to the $U_{\mathrm{eff}}$ are generally "isotropic" in that they are based solely on the occupation. The marked improvement by the $U|J$ method emphasises the importance of explicit spatial exchange anisotropy in the LaMnO₃ Mn $d$ manifold. The results in Table III are encouraging, but since distortion of the lattice is critical in LaMnO₃,[2] the trends observed must

be verified by fully relaxing ionic positions and lattice parameters, which we report on next.

### 4. Relaxed LaMnO₃ structure *via* DFT+$U|J$

Table IV displays key data for fully relaxed bulk LaMnO₃ using the DFT+$U|J$ framework. Relaxed results largely echo the experimental structure results above for A-AFM LaMnO₃, with the $U|J$ combination of $U = 8$ eV and $J = 2$ eV providing a good material description. In particular the $U|J = 8|2$ eV combination provides agreement in terms of electronic, magnetic and structural observables from experiment[44,46,47,51] and also more computationally expensive many body GW approximation[52] results. Volume errors < 1 % improve on previous work,[23,44,51] and the error in energy gap is small at approximately ~ 5 % (< 0.1 eV error)[46] In addition the A-AFM ordering is stabilized against

Table III: Results from GGA (PBEsol) + $U|J$ for the experimental geometry of bulk LaMnO$_3$. Band gaps $E^{\mathrm{Gap}}$ are in eV for each magnetic state, and $\Delta E = E^{\mathrm{A\text{-}AFM}} - E^{\mathrm{FM}}$ is the total energy difference per unit cell between the two magnetic phases.

| $U|J$ (eV) | $E^{\mathrm{Gap}}_{\mathrm{A\text{-}AFM}}$ (eV) | $E^{\mathrm{Gap}}_{\mathrm{FM}}$ (eV) | $\Delta E$ (meV) |
|---|---|---|---|
| 6\|0 | 1.3 | 0.1 | 14 |
| 6\|1 | 1.3 | 0.2 | 6 |
| 6\|2 | 1.2 | 0.4 | -10 |
| 6\|3 | 0.6 | 0.2 | -39 |
| 8\|0 | 1.4 | 0.2 | 17 |
| 8\|1 | 1.5 | 0.4 | 11 |
| 8\|2 | 1.6 | 0.8 | -2 |
| 8\|3 | 1.0 | 0.5 | -32 |

FM ordering which was previously seen as a missing ingredient[23,24]. The improvements in LMO description depend intimately on the intra-orbital exchange description - this is explored further by quantifying the action of the Hund's coupling interaction on the LMO Mn $d$ states.

## B. Explicit exchange anisotropy in Mn$^{3+}$

Strong on-site Coulomb repulsion is the central theme in paradigms of "Mottness" and electron localisation. However, the importance of Hund's coupling (intra-orbital exchange) in materials with partial $d$ and $f$-shell occupations has been highlighted.[53] In this section, we attempt to understand the nature of Hund's coupling in LMO, by examining the effects of the on-site exchange terms as defined in Appendix A. We explore why the $U|J$ methodology can describe LaMnO$_3$ adequately, reproducing band gap and correct magnetic ground state simultaneously. We employ a simple model where we focus only on the occupancies of the Mn$^{3+}$ $d^4$ manifold in order to isolate the effect of the exchange $J$ parameter (and related physics) on the Mn $d$ states as per Equation (4). Majority spin $t_{2\mathrm{g}}{}^3$ states are generally fully occupied due to the strong exchange splitting between spin channels, and as is well known, increasing $U$ increases occupancy polarization. However the nature of anisotropic interactions in the Mn $d$ shell due to $J$ is less well understood, particularly with respect to the polarization of the $e_{\mathrm{g}}{}^1$ occupation into $3z^2 - r^2$ or $x^2 - y^2$ (or some mix of the two).

We begin with three model $e_{\mathrm{g}}{}^1$ occupations, $\pi^{e_{\mathrm{g}}} = 0, \pm 1$, in an attempt to pinpoint what $J$ really does and understand the nature of Hund's coupling in different limits. As a reminder, $\pi^{e_{\mathrm{g}}}$ is the $e_{\mathrm{g}}$ occupancy polarization as defined in Equation (1). After examining these model systems, we will consider the effect of $J$ in the actual calculations where we use the calculated *ab initio* occupations together with our analytical rewriting of the $U|J$ energy function and eigenvalue corrections. As explained above, the $e_{\mathrm{g}}$ and $t_{2\mathrm{g}}$ group terms discussed correspond to the local octahedral basis (*i.e.*, post rotation as per Appendix B).

### 1. Anisotropic exchange for model orbital occupations

To illustrate the anisotropic effects of the $J$ terms in the $U|J$ schema, we begin with a set of model occupancies where we fix the formal occupation of Mn$^{3+}$ ($d^4$) but vary the orbital polarization.

A $\pi^{e_{\mathrm{g}}} = +1$ model polarization corresponds to a single hole on the majority spin $3z^2 - r^2$ site (*i.e.*, $f_{x^2-y^2\sigma} = f_{t_{2\mathrm{g}}\sigma} = 1$, $f_{3z^2-r^2\sigma} = 0$ and $f_{\bar\sigma} = 0$). Based on Equation (4), the added effect of the exchange $J$ terms is to create additional energy splittings (beyond simple occupancy polarization proportional to $U_{\mathrm{eff}}$) given by

$$\pi^{e_{\mathrm{g}}} = +1 \ : \quad (\triangle\epsilon_\sigma | \triangle\epsilon_{\bar\sigma}) = J \cdot \begin{pmatrix} 0.00 & -1.14 \\ 0.52 & 0.63 \\ 0.52 & 0.63 \\ -0.52 & -0.06 \\ -0.52 & -0.06 \end{pmatrix}. \quad (6)$$

The opposite polarity, $\pi^{e_{\mathrm{g}}} = -1$, corresponds to a single hole on the majority spin $x^2 - y^2$ site (that is, $f_{3z^2-r^2\sigma} = f_{t_{2\mathrm{g}}\sigma} = 1$, $f_{x^2-y^2\sigma} = 0$ and $f_{\bar\sigma} = 0$). This results in the following exchange energy splittings

$$\pi^{e_{\mathrm{g}}} = -1 \ : \quad (\triangle\epsilon_\sigma | \triangle\epsilon_{\bar\sigma}) = J \cdot \begin{pmatrix} 0.52 & 0.63 \\ 0.00 & -1.14 \\ -0.86 & -0.29 \\ 0.17 & 0.40 \\ 0.17 & 0.40 \end{pmatrix}. \quad (7)$$

Removing the polarization, $\pi^{e_{\mathrm{g}}} = 0$, the single hole is equally spread over the two majority spin $e_{\mathrm{g}}$ sites ($f_{e_{\mathrm{g}}\sigma} = 0.5$ and $f_{t_{2\mathrm{g}}\sigma} = 1$ and $f_{\bar\sigma} = 0$). This leads to the splittings

$$\pi^{e_{\mathrm{g}}} = 0 \ : \quad (\triangle\epsilon_\sigma | \triangle\epsilon_{\bar\sigma}) = J \cdot \begin{pmatrix} 0.26 & -0.26 \\ 0.26 & -0.26 \\ -0.17 & 0.17 \\ -0.17 & 0.17 \\ -0.17 & 0.17 \end{pmatrix}. \quad (8)$$

To visualize these results, we display a schematic showing these splittings in these three cases of $\pi^{e_{\mathrm{g}}} = 0, \pm 1$ in Figure 3 where the corrections due to both $U$ and $J$ are shown.

These model results together with the Figure 3 clearly point out that the effect of the $J$ terms is explicitly anisotropic and its anisotropy and precise value depends on the orbital polarization (which may have been present due the action of the $U_{\mathrm{eff}}$ term). The anisotropy exists across both the magnetic quantum number and spin

Table IV: Fully relaxed LaMnO$_3$ results based on GGA (PBEsol) + $U|J$. Band gaps $E^{\text{Gap}}$, lattice parameter errors, and total energy differences between the A-AFM and FM magnetic phases $\Delta E = E^{\text{A-AFM}} - E^{\text{FM}}$ per formula unit are listed.

| $U\|J$ (eV) | A-AFM | | | | | $\Delta E$ (meV) |
| --- | --- | --- | --- | --- | --- | --- |
| | $E^{\text{Gap}}$ (eV) | $\Delta^{\text{a}}$ (%) | $\Delta^{\text{b}}$ (%) | $\Delta^{\text{c}}$ (%) | $\Delta^{\text{Vol.}}$ (%) | |
| 6\|0 | 1.1 | 0.4 | -0.1 | -0.4 | 0.0 | 19 |
| 6\|0.5 | 1.2 | 0.6 | -0.4 | -0.4 | -0.2 | 14 |
| 6\|1 | 1.3 | 0.9 | -0.7 | -0.5 | -0.3 | 7 |
| 6\|1.5 | 1.4 | 1.2 | -0.9 | -0.6 | -0.3 | -1 |
| 6\|2 | 1.4 | 0.8 | -1.2 | 0.1 | -0.4 | -10 |
| 6\|2.5 | 1.3 | 1.8 | -1.3 | -0.8 | -0.2 | -21 |
| 7\|0 | 1.2 | 0.5 | 0.1 | -0.3 | 0.3 | 23 |
| 7\|0.5 | 1.3 | 0.7 | -0.2 | -0.4 | 0.2 | 17 |
| 7\|1 | 1.4 | 0.9 | -0.5 | -0.5 | 0.0 | 11 |
| 7\|1.5 | 1.5 | 1.2 | -0.7 | -0.5 | -0.1 | 3 |
| 7\|2 | 1.6 | 1.6 | -1.0 | -0.7 | 0.0 | -6 |
| 7\|2.5 | 1.5 | 1.9 | -1.2 | -0.7 | -0.1 | -17 |
| 8\|0 | 1.1 | 0.5 | 0.4 | -0.3 | 0.6 | 27 |
| 8\|0.5 | 1.2 | 0.6 | 0.1 | -0.3 | 0.4 | 21 |
| 8\|1 | 1.4 | 1.0 | -0.2 | -0.5 | 0.3 | 15 |
| 8\|1.5 | 1.6 | 1.2 | -0.5 | -0.5 | 0.1 | 7 |
| 8\|2 | 1.8 | 1.5 | -0.8 | -0.6 | 0.1 | -2 |
| 8\|2.5 | 1.7 | 1.7 | -1.0 | -0.6 | 0.1 | -14 |

channels ($\sigma$ and $\bar{\sigma}$). We now discuss these three cases in more detail.

When we have full $e_{\text{g}}$ orbital polarization, *i.e.* $\pi^{e_{\text{g}}} = \pm 1$, each polarity produces a unique splitting pattern where the magnitude of anisotropy depends on the sign of $\pi^{e_{\text{g}}}$. This is despite the fact that $3z^2 - r^2$ and $x^2 - y^2$ states both have $e_{\text{g}}$ symmetry: as we can see that occupying each one (separately) splits the $t_{2\text{g}}$ quite differently. This difference is due to fact that the $x^2 - y^2$ state is symmetry related to the $t_{2\text{g}}$ states (it is the $xy$ state rotated by $\pi/4$ about the $z$ axis). For example, when $x^2 - y^2$ is fully occupied, the splittings for $x^2 - y^2$ and $xy$ are identical but differ from the other orbitals, but same is not true when $3z^2 - r^2$ is filled instead. Interestingly $\sum_{i\sigma} \Delta \epsilon_{i\sigma} f_{i\sigma} = 0$ when $\pi^{e_{\text{g}}} = \pm 1$: this indicates that neither polarization is energetically preferred by intra-orbital $J$ terms.

With zero $e_{\text{g}}$ orbital polarization, *i.e.* $\pi^{e_{\text{g}}} = 0$, we find that this degeneracy inhibits anisotropy from the $J$ terms: the splitting *within* each $t_{2\text{g}}$ and $e_{\text{g}}$ manifold is isotropic for both spin channels. The action of the $J$ terms in this situation is to shift the energies of this manifold *en masse*. Here, $\sum_{i\sigma} \Delta \epsilon_{i\sigma} f_{i\sigma} = -0.26 J$ when $\pi^{e_{\text{g}}} = 0$ compared to zero for $\pi^{e_{\text{g}}} = \pm 1$. Hence, the anisotropic exchange terms in isolation actually favour degenerate occupancy. This result appears to be counterintuitive given the importance of $J$ to anisotropy. The resolution is that we have a much larger and dominant direct Coulomb term $U$ that produces orbital polarization in the first place; the weaker $J$ terms then further enlarge the polarization and make the system more anisotropic. Table V shows this behaviour numerically.

In brief, we see that $J$ acting alone energetically *favours degeneracy*. However, with a strong $U$ term already creating orbital polarization, the $J$ terms provide the enlarged anisotropic splitting that one finds in the final results of the calculation.

### 2. Anisotropic exchange for ab initio orbital occupations

For the *ab initio* orbital occupations we use the DFT+$U|J = 8|2$ eV calculation results, which yield an occupation-polarized $e_{\text{g}}$ manifold as shown in Table V. The $e_{\text{g}}$ polarity is found to be orbitally ordered across the LaMnO$_3$ unit cell as shown in Figure 4. We now examine this situation in more detail.

The Mn $d$ occupancies from the $U|J = 8|2$ eV method with relaxed geometry are

$$(f_\sigma | f_{\bar{\sigma}}) = \begin{pmatrix} 0.99 & 0.10 \\ 0.41 & 0.33 \\ 0.98 & 0.06 \\ 0.96 & 0.04 \\ 0.97 & 0.05 \end{pmatrix}. \tag{9}$$
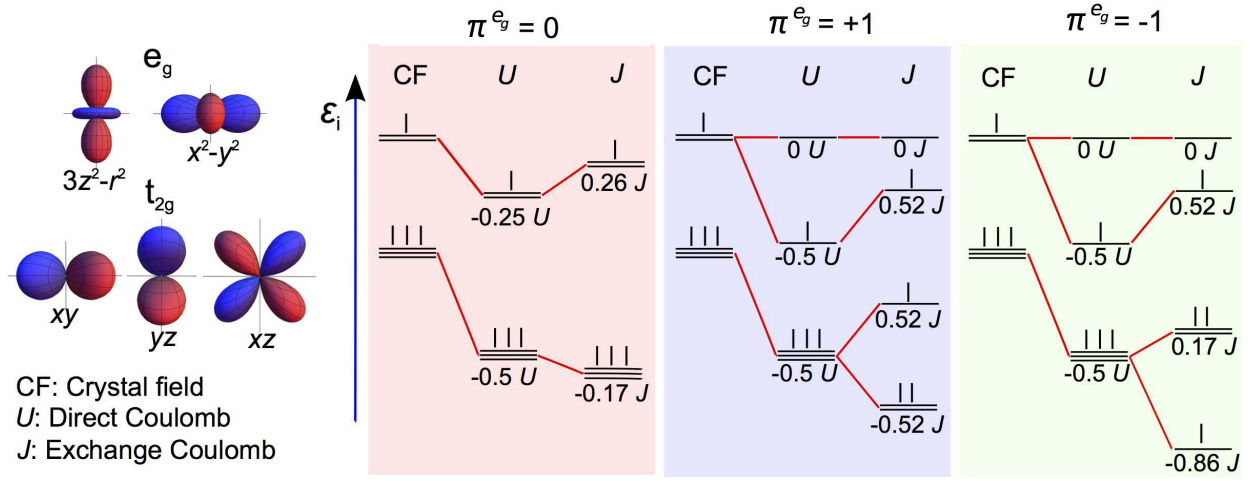
Figure 3: The occupation of states is represented in the model $Mn^{3+}$ $d^4$ manifold (majority spin only). Orbital degeneracy is broken by octahedral crystal field (CF), Coulomb repulsion $U_{eff}$ ($U$ in the figure) and exchange $J$ following Equation (4). Each vertical bar represents one unit of electron occupation. $\pi^{e_g\sigma}$ (denoted $\pi^{e_g}$ for the majority spin channel in the figure) is defined in Equation (1), and three limits are examined: $\pi^{e_g\sigma} = 0$ ($f_{x^2-y^2\sigma} = f_{3z^2-r^2\sigma} = 0.5$), $\pi^{e_g\sigma} = +1$ ($f_{x^2-y^2\sigma} = f_{3z^2-r^2\sigma} + 1 = 1$), and $\pi^{e_g\sigma} = -1$ ($f_{x^2-y^2\sigma} + 1 = f_{3z^2-r^2\sigma} = 1$).
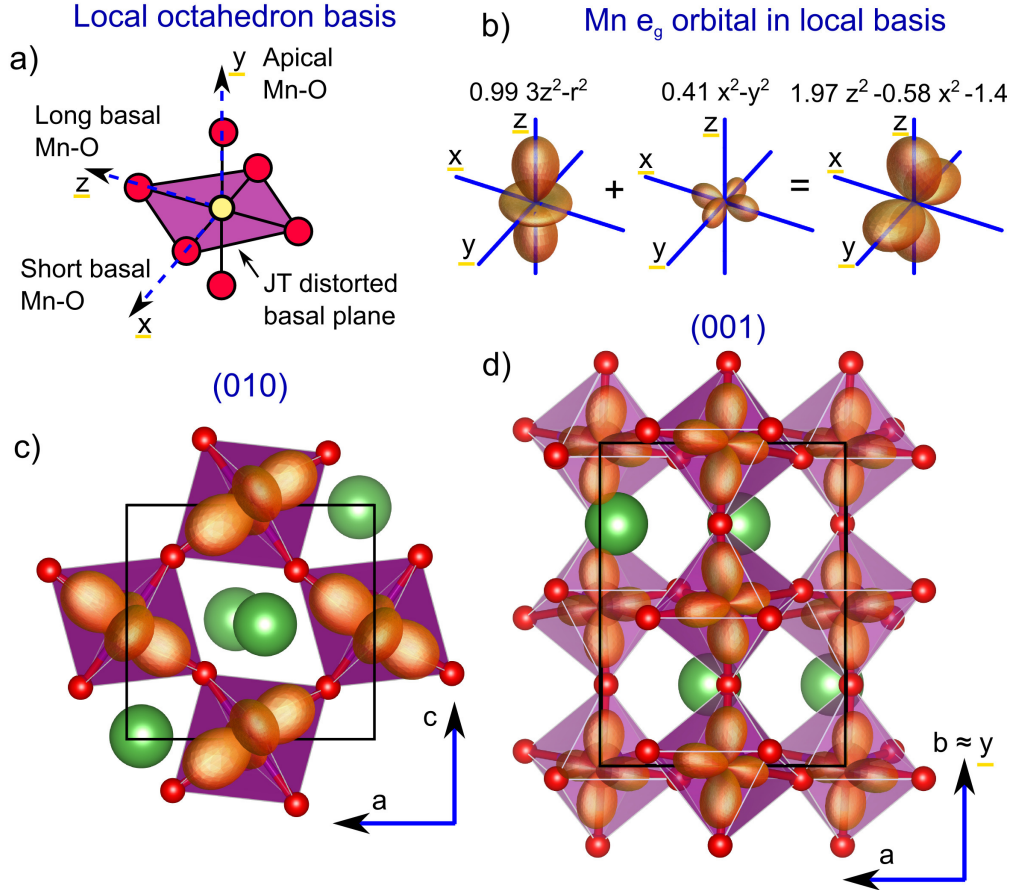


Figure 4: Orbitals in the $LaMnO_3$ unit cell from a $U|J = 8|2$ eV calculation. a) $MnO_6$ octahedron with Jahn-Teller distorted plane and local basis vectors labelled. b) Visualization of the occupation of the $3z^2 - r^2$ and $x^2 - y^2$ states in the rotated basis of the density matrix as well as their superposition for the total local $e_g$ occupancy (plotting the occupation times the orbital expressed in spherical harmonics). c) The ordering of the occupied $e_g$ shell ($1.97z^2 - 0.58x^2 - 1.4y^2$) in the (010) Jahn-Teller distorted FM coupled plane. d) The ordering of the occupied $e_g$ shell in the (001) plane with AFM coupling along $b$. Note $x, y, z$ is the local octahedron basis, and $a, b, c$ lattice vectors correspond to $x', y', z'$ global (pre-rotation) calculation basis.

These occupancies correspond to $\pi^{e_g\sigma} = -0.41$ (from $f_{3z^2-r^2\sigma} = 0.99$ and $f_{x^2-y^2\sigma} = 0.41$). The Mn $d$ shell obviously has more electrons than the model system above which was based on formal occupancies for $Mn^{3+}$. Again, we note that this increase is due to hybridization of the Mn $d$ orbitals with the neighboring O $2p$ orbitals which admixes some Mn $d$ into the low-energy occupied valence states and increases the electron count. Put differently, itineracy due to the kinetic energy minimization competes with Hubbard-esque Coulomb repulsion and we reach a balance. Numerically, for $U|J = 8|2$ eV, the oxidation state based on the above Mn $d$ occupations can be calculated to be 2.12+ (an alternative or complementary Bader charge picture yields an oxidation state of 1.68+, still less than the formal 3+).

The $U|J = 8|2$ eV occupancies of Equation (9) result in energy splitting beyond splitting from $U_{\text{eff}}$ alone:

$$(\triangle\epsilon_\sigma|\triangle\epsilon_{\bar\sigma}) = J \cdot \begin{pmatrix} 0.15 & 0.20 \\ 0.30 & -0.65 \\ -0.41 & -0.06 \\ -0.03 & 0.18 \\ -0.01 & 0.20 \end{pmatrix}. \quad (10)$$

The $e_g$ occupancy polarization of the $U|J = 8|2$ eV calculation is considerably weaker than the previous model cases. Nevertheless, it is large enough to drive significant anisotropic exchange splittings in Equation (10). For example, the splittings are anisotropic within the majority spin $t_{2g}$ manifold: the $xy$ state is pushed down by approximately $0.4J$ compared to the other two $t_{2g}$ states. Within the $e_g$ manifold, the fully occupied $3z^2-r^2$ state is pushed up by $0.15J$ while the partially occupied $x^2-y^2$ state is pushed up considerably more by $0.30J$.

The direct Coulomb interaction $U$ obviously increases $\pi^{e_g}$, as expected from the standard instability condition for orbital polarization[23,54],

$$U_{\text{eff}} \times D^\sigma(E_F) \gg 1,$$

where $D^\sigma(E_F)$ is the density of states in the $\sigma$ spin channel at the Fermi level. The origin of the monotonic relation between $\pi^{e_g}$ and $J$, shown in Table V, is less obvious as $J$ is naïvely expected to drive the electronic structure away from orbital polarization as $U_{\text{eff}} = U - J$. However $\pi^{e_g}$ does increase with $J$, for the above-noted reason that $J$ alone may favour orbital degeneracy but $J$ is strongly anisotropic when in conjunction with a large $U$ value, resulting in the unequal upward "push" of the two $e_g$ orbitals with increasing $J$. That $J$ and $\pi^{e_g}$ are so strongly coupled in this material is interesting, as band gap, Jahn-Teller distortions, and inter-site magnetic couplings all depend on $\pi^{e_g}$.

As first examined by Kugel and Khomskiĭ,[55] $e_g{}^1$ occupation polarization (i.e., an electron-electron Jahn-Teller degeneracy breaking) enhances virtual superexchange interactions, relative to kinetic exchange interactions such as FM double-exchange. This competition

Table V: Orbital occupation polarization, $\pi^{e_g\sigma}$, for fully relaxed LaMnO$_3$ within the $U_{\text{eff}}$ and $U|J$ approaches. Majority spin are $\sigma$ and minority spin are $\bar\sigma$.

| Correction (eV) | Like-spin polarization, $\pi^{e_g\sigma}$ | Opposite-spin polarization, $\pi^{e_g\bar\sigma}$ |
|---|---|---|
| $U_{\text{eff}} = 0$ | 0.06 | 0.08 |
| $U_{\text{eff}} = 8$ | $-0.27$ | 0.25 |
| $U|J = 8|1$ | $-0.33$ | 0.41 |
| $U|J = 8|2$ | $-0.41$ | 0.54 |
| $U|J = 8|3$ | $-0.52$ | 0.65 |

between superexchange and double-exchange is observed in the LMO magnetic ground state, which varies according to the magnitude of $\pi^{e_g}$ ($e_g$ occupancy polarization). $\pi^{e_g}$ increases with $J$, which explains the flip in long range magnetic ordering of the ground state from FM to A-AFM as the intra-orbital parameter $J$ is increased.

At $J = 2$ eV the value of $\pi^{e_g}$ in Table V is large enough to stabilize the correct A-AFM ordering (as per Table IV). The $U|J = 8|2$ A-AFM ground state in Figure 1 corresponds to a $0.99(3z^2 - r^2) + 0.41(x^2 - y^2)$ $e_g$ occupation density in the local octahedral basis. The orbital ordering pattern across the unit cell is shown in Figure 4, and can be rationalized in terms of the Goodenough-Kanamori superexchange rules.[56,57]

The $0.99(3z^2-r^2)+0.41(x^2-y^2)$ $e_g$ occupation density can be rewritten as $1.97z^2 - 0.58x^2 - 1.4y^2$. This expression shows the anisotropy in the $e_g$ state, in particular between the $z$ and $x$ directions in the octahedron: the $z^2$ contribution is much larger than $x^2$, as per Figure 4 b. Each octahedral frame in the $ac$ plane is related to its neighbour by a $\pi/2$ rotation about the $b$ lattice vector, so $z^2/x^2$ anisotropy forms a checker board pattern of $e_g$ partial occupation in the $ac$ plane. Note this corresponds to the long/short Jahn-Teller Mn-O pattern in the $ac$ plane, as per Figure 4 c). According to the Goodenough-Kanamori rules, superexchange in the $ac$ plane is determined by $z^2/x^2$ anisotropy in the $e_g$ partial occupation, and results in the FM coupling in the $ac$ plane.

The $y^2$ component of the $e_g$ partial occupation forms occupied stripes pointed along local octahedra y axes, following the $b$ lattice direction (with a small tilt) as in Figure 4 d). The continuous stripes of $y^2$ character along the $b$ lattice direction correspond to the 'non-Jahn-Teller' Mn-O bonds in this direction. The Goodenough-Kanamori rules determine that the continuous stripe of $y^2$ character from the $e_g$ partial occupation corresponds to AFM superexchange. The AFM coupling is along the $b$ lattice parameter direction, between the FM coupled $ac$ planes. Together the in-plane FM and inter-plane AFM produce the A-AFM ground state of LaMnO$_3$, so our $U|J = 8|2$ eV calculation results are in-line with experiment as well.

If instead the Hund's coupling was weaker (i.e., smaller $J$), then $\pi^{e_g}$ would also be smaller. This alters the char-
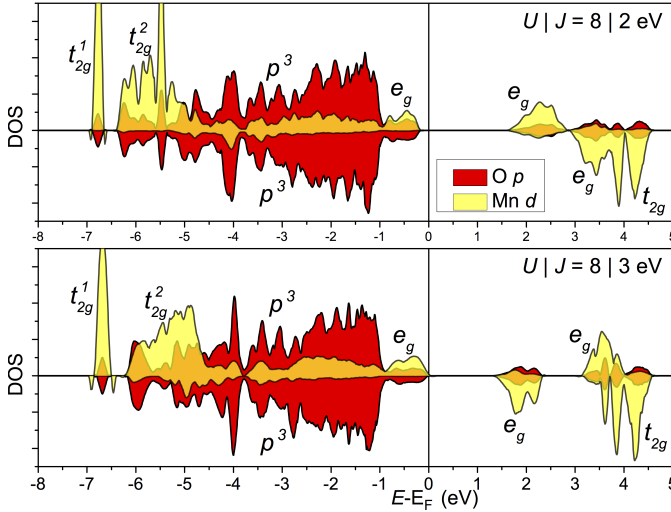
Figure 5: LaMnO$_3$ densities of states (DOS) for $U|J = 8|2$ eV and $U|J = 8|3$ eV calculations. Majority spin corresponds to positive DOS and minority to negative DOS.



Figure 6: Local magnetic moment within the Bader volume for Mn cations and O anions (within the (010) basal plane), from DFT+$U_{\text{eff}}$ and DFT+$U|J$ methods. The notation $U_6|J$ and $U_8|J$ indicates $U$ is fixed to 6 eV and 8 eV, respectively, while $J$ is varied. The experimental reference local magnetic moment is 3.7 $\mu_B$.[51]

acter of the occupied states in the $e_{\text{g}}$ shell, so that orbital-ordering mediated A-AFM superexchange is reduced relative to other effects such as FM double-exchange. This explains why stabilization of A-AFM magnetic ordering (see Table IV) is only possible when intra-orbital exchange is large enough. Too small of an intra-orbital exchange interaction is the origin of the incorrect FM ground state found in prior examinations[2,23,24] of LMO using standard DFT.

The improvements in the LMO description through applying exchange corrections reinforce hints by Sawada *et al.*,[23] Solovyev *et al.*[2] and Hashimoto *et al.*,[24] that the correct orbital and magnetic ordering in LMO requires an anisotropic intra-orbital exchange correction to the DFT ground state. In what follows, we discuss further details of the electronic and crystal structure.

### C. Electronic and crystal structure details

#### 1. Orbital order

It was previously shown that applying Coulomb corrections, such as with $U|J = 8|2$ eV, corrected the LMO electronic, magnetic and lattice structure. Further electronic structure details are shown for the LMO DOS in Figure 5 at the $U|J = 8|2$ eV level of correction. In Figure 5 the position of each band in the Mn DOS agree quantitatively with the optical conductivity measurements of Jung *et al.*.[47] Further experimental agreement comes from our $U|J = 8|2$ eV calculated local magnetic moment, which at $3.7\mu_B$ agrees with Eleman's measurement.[51] The $U$ and $J$ dependence of the local magnetic moments are shown in Figure 6. The high sensitivity of the electronic structure of LMO to perturbations in part underlies its complex phase dia-
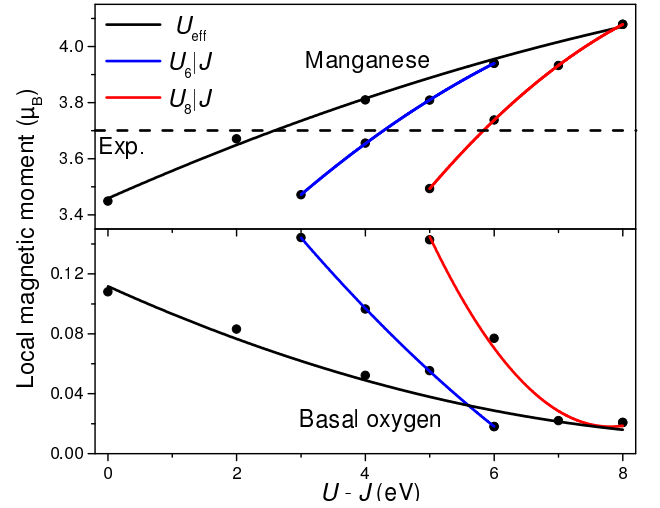
gram. This is illustrated by comparing the $U|J = 8|2$ and $U|J = 8|3$ eV DOS in Figure 5, and examining the magnetic state of DOS near the edges of the valence band maximum (VBM) and conduction band minimum (CBM). For $U|J = 8|2$ eV, Hund's rules are obeyed as both VBM and CBM have the same spin state whereas Hund's rules are broken for $U|J = 8|3$ eV. We find that the cross-over occurs at $J \approx 2.4$ eV. LaMnO$_3$ is fragile in terms of exchange: above $J \approx 2.4$ eV we have the breakdown of Hund's rules while below $J \approx 1.8$ eV incorrectly stabilizes the FM rather than A-AFM ground state.

#### 2. Magnetic coupling constants

The magnetic coupling constants in LMO have been extracted by Muñoz *et al.*[20] amongst others[2,24,49,58], by considering an Ising model (with $S = 2$ spin moment per Mn ion) for different spin-ordered solutions. The intra-plane ($ac$) $J_1$ and inter-plane ($b$) $J_2$ coupling constants for the 20 atom LMO unit cell are

$$J_1 = \frac{1}{64} \left[ E^{\text{G-AFM}} - E^{\text{A-AFM}} \right]$$
$$J_2 = \frac{1}{32} \left[ E^{\text{A-AFM}} - E^{\text{FM}} \right] . \quad (11)$$

The initial A-AFM/FM stability results in Table IV hint that the coupling constants will depend strongly on the Hund's exchange parameter. In the context of previous works, $J_i$ are well known to be highly sensitive, for example to variation in Mn-O-Mn angle through

superexchange interactions[59], and the Mn ionic charge population[58].

On the trend of magnetic stability in $U$ and $J$, the superexchange interaction which stabilizes AFM ordering is expected to scale inversely with effective on-site Coulomb interaction, $i.e.$ $\sim t^2/U_{\mathrm{eff}}$ where $t$ is effective inter-site hopping. Considering first $J_2$ ($\sim E^{\mathrm{A\text{-}AFM}} - E^{\mathrm{FM}}$) in Figure 7, the stability of AFM coupling along $b$ decreases both with increasing $U$ or decreasing $J$ as expected since $U_{\mathrm{eff}} = U - J$. However, the dependence of the $J_2$ coupling on $U$ and $J$ is not equivalent: the variation in $J_2$ is some five-fold more sensitive to changes in $J$ than $U$, $i.e.$, $\partial J_2/\partial J \approx -5\partial J_2/\partial U$. The AFM coupling in the $ac$ plane, measured by $J_1$, is even more sensitive to the intra-orbital Hund's parameter, with $\partial J_1/\partial J \approx -10\partial J_1/\partial U$. The origin of coupling constant sensitivity to $J$, is the strongly anisotropic effect of $J$ on the LMO Mn $d$ shell states, with variation in $J$ increasing $\pi^{e_g}$ in Table V above and beyond that accesible with $U$ alone.

Neutron scattering experiments have determined coupling constant values of $J_1^{\mathrm{exp}} = 0.83$ meV and $J_2^{\mathrm{exp}} = -0.58$ meV.[60] In Figure 7 reasonable values for $J_1$ are produced with $J \approx 1.75$ eV, and for $J_2$ with $J_2 \approx 2$ eV. The discrepancy in $J$ value for each $J_i$ is perhaps unsurprising given the extreme sensitivity of A-AFM, G-AFM and FM phases to the intra-orbital Hund's interaction. Overall the $U|J = 8|2$ eV combination previously suggested remains a good compromise at the level of half integer eV screening intervals considered here. Although higher resolution screening in $J$ is beyond the scope of this work, if DFT+$U|J$ calculations are required for thermodynamics applications, results indicate a small modification of $J$ by a few percent may be advantageous to tune the magnetic transition temperatures precisely, while the magnetic couplings are relatively insensitive to the direct $U$ term.

Due to the sensitivity of the magnetic couplings to the Coulombic $J$ correction, agreement with experiment is challenging. At the $U = 8$ eV required to open the band gap, and screening in $J$ at half integer intervals shown in Figure 7, $U|J = 8|2$ eV remains the best compromise. For $U|J = 8|2$ eV the inter-plane coupling at $J_2 = -0.30$ meV has the correct sign but in magnitude falls short of $J_2^{\mathrm{exp}} = -0.58$ meV[60]. More problematic is the intra-plane coupling, which overestimates the tendency for electrons to couple antiferromagnetically in the $ac$ plane, excessively stabilizing G-AFM ordering at $J_2 = -0.19$ meV compared to $J_2^{\mathrm{exp}} = +0.83$ meV.

In Figure 7 the colored areas show the $J$ values that correspond to coupling constants between zero and $J_i^{\mathrm{exp}}$, $i.e.$ the correct sign for each $J_i$. The overlap in colored areas identifies the narrow range of intra-orbital exchange values, $1.88 \leq J \leq 1.95$ eV, that gives the correct signs for both $J_i$ together, with $E(\mathrm{A\text{-}AFM}) < E(\mathrm{FM}) < E(\mathrm{G\text{-}AFM})$ in agreement with experiment[60]. Based on the refinement in $J$ value, we have performed GGA (PBEsol) calculations with $U|J = 8|1.9$ eV. The error in calculation results with respect to experimen-
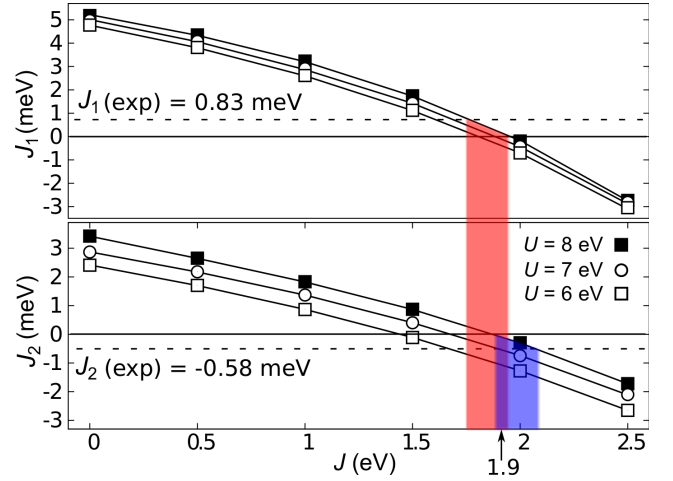


Figure 7: LaMnO$_3$ magnetic coupling constants $J_1$ and $J_2$ versus $U|J$ schema Hund's exchange parameter $J$, for $U = 6$ eV (white squares), $U = 7$ eV (white circles), $U = 8$ eV (black squares). $J_1$ and $J_2$ are defined in Equation (11). The red-blue overlap (centered at $J = 1.9$ eV) suggests a $J$ exchange value for the $U|J$ scheme that provides the correct sign for both coupling constants - see main text for discussion.

tal values[44,47,51,60–62] is summarized in Table VI. The $U|J = 8|1.9$ eV calculations produce good experimental agreement overall, with magnetic coupling constants with signs that agree with experiment, $J_1 = +0.2$ and $J_2 = -0.1$ meV, a band gap value only a couple of percent above the experimental 1.7 eV value, lattice parameter errors between $+1.5$ % and $-0.8$ % which largely cancel to give a volume error with respect to experiment of $+0.1$ %.[47,60]

### 3. Jahn-Teller distortion

We end our analysis with conclusions on the nature of Jahn-Teller distortion in LMO and on the origin of the LMO insulating state. Jahn-Teller distortion in LaMnO$_3$ can be characterized in terms of two normal modes of the type introduced by van Vleck[63] and by Kanamori[64]. The normal modes are shown in Figure 8 along with the crystal unit cell and the local octahedral basis. The modes are calculated as

$$\mathbf{Q}^{\mathrm{Ortho}} = \frac{1}{\sqrt{2}} \left[ \mathbf{Y}_2 - \mathbf{Y}_5 - \mathbf{X}_1 + \mathbf{X}_4 \right]$$

$$\mathbf{Q}^{\mathrm{Tetra}} = \frac{1}{\sqrt{6}} \left[ 2\mathbf{Z}_3 - 2\mathbf{Z}_6 - \mathbf{Y}_2 + \mathbf{Y}_5 - \mathbf{X}_1 + \mathbf{X}_4 \right].$$

Each variable represents an octahedral bond length, with subscripts indexing oxygen octahedral cage sites for a given manganese centre, $i$ ($i = 1, ...6$). In the local basis in this work, which differs from other choices[24,49,65], $\mathbf{Z}_i = \mathbf{z}_i^{\mathrm{O}} - \mathbf{z}^{\mathrm{Mn}}$ are the long Mn-O bonds and $\mathbf{X}_i = \mathbf{x}_i^{\mathrm{O}} - \mathbf{x}^{\mathrm{Mn}}$ short Mn-O bonds, with both in the FM coupled $ac$

Table VI: LaMnO$_3$ electronic, magnetic and structural properties obtained from a $U|J = 8|1.9$ eV calculation, with comparison to experimental counter-parts.[44,47,51,60–62] The $J = 1.9$ eV value is based on a refinement of the Hund's exchange parameter to secure the correct sign for both magnetic coupling constants, $J_1$ and $J_2$, which are exceptionally sensitive to on-site exchange - see Figure 7.

| $U|J$ (eV) | Electronic gap | | Magnetic | | | Structural | | |
|---|---|---|---|---|---|---|---|---|
| | $E$ $^{\mathrm{Gap}}$ (eV)[47] | Character[47] | $J_1$, $J_2$ (meV)[62] | $M$ ($\mu_B$)[51] | $\mathbf{Q}^{\mathrm{Ortho}}$, $\mathbf{Q}^{\mathrm{Tetra}}$ (a.u.)[44] | $a$, $b$, $c$ (Å)[44] | $V$ (Å$^3$)[44] |
| 8|1.9 | 1.75 | $e_{g\uparrow}^1 \to e_{g\uparrow}^2$ | +0.2, −0.1 | 3.76 | 0.145, 0.856 | 5.823, 7.642, 5.508 | 245 |
| Exp. | 1.7 | $e_{g\uparrow}^1 \to e_{g\uparrow}^2$ | +0.83, −0.58 | 3.7 | 0.14, 0.78 | 5.736, 7.703, 5.540 | 245 |

plane. $\mathbf{Y}_i = \mathbf{y}_i^{\mathrm{O}} - \mathbf{y}^{\mathrm{Mn}}$ are along the inter-plane AFM coupled $b$ lattice direction.

We begin commenting that the formation of a band gap in LaMnO$_3$ is not solely electron-electron ($e$-$e$) or electron-lattice ($e$-$l$) in character. Rather, it is a joint function of the lattice relaxation and development of Jahn-Teller distortions as well as the strong on-site Coulomb interaction. This is illustrated explicitly in Figure 8. As mentioned above, two logically distinct routes to breaking symmetry exist in order to produce a gap: (i) a purely electronic effect $via$ electron-electron interactions and the formation of a sizable orbital polarization $\pi^{e_g}$ that breaks symmetry (also called $e$-$e$ Jahn-Teller distortion)[55], or (ii) electron-lattice ($e$-$l$) Jahn-Teller distortions where certain local octahedral phonon modes become soft, the Mn-O bond lengths become unequal, and this creates crystal field symmetry breaking. These two mechanisms are in fact mutually enhancing, and which one causes which in LaMnO$_3$ is an open question that has been debated in the works of Khomskii[66], Yin $et$ $al.$[67], and Loa $et$ $al.$[7].

In some materials, one mechanism can clearly dominate over the other. For example, in KCuF$_3$, to which LaMnO$_3$ is superficially similar as both are perovskites with partial $e_g$ occupation, the symmetry lowering is truly driven by electronic interactions alone,[22] and thus KCuF$_3$ is said to exhibit $e$-$e$ Jahn-Teller distortion. Figure 8 shows that the nature of Jahn-Teller is different in LaMnO$_3$.

Firstly, with the $e$-$l$ distortion frozen out, one can generate symmetry breaking and a gap for a Coulomb interaction strength $(U - J)$ above a critical value $\sim 2$ eV, so that in principle, the lattice distortion is not necessary to create a gap. However, in practice, the gap and orbital splitting remain small without lattice Jahn-Teller distortions. Secondly, with $U - J$ set to zero, the DFT calculations do produce weakly active $e$-$l$ Jahn-Teller distortions of $\mathbf{Q}^{\mathrm{Ortho}} = -0.02$ a.u. and $\mathbf{Q}^{\mathrm{Tetra}} = 0.14$ a.u., but the gap remains essentially zero. The addition of Coulomb repulsion $via$ $U_{\mathrm{eff}}$ greatly enhances the $e$-$l$ distortion of each mode to approximately $\mathbf{Q}^{\mathrm{Ortho}} \approx 0.12$ a.u. and $\mathbf{Q}^{\mathrm{Tetra}} \approx 0.62$ a.u.. However even with $U_{\mathrm{eff}}$ applied $\mathbf{Q}^{\mathrm{Ortho}}$ and $\mathbf{Q}^{\mathrm{Tetra}}$ remain still short of experiment by some 13 % and 20 % respectively. As per Table V and Figure 8, one can only go so far with $U_{\mathrm{eff}}$: the orbital polarization $\pi^{e_g}$ is too weak and the Jahn-Teller $e$-$l$ distortion remains largely unchanged with increasing $U_{\mathrm{eff}}$.

The only way to bridge the deficit is through the use of a dedicated exchange term $via$ the $U|J$ approach. As shown in Table V, $J$ increases $\pi^{e_g}$ and anisotropy throughout the $d$ manifold significantly. By increasing $J$ in the $U|J$ scheme, the LMO $\mathbf{Q}^{\mathrm{Ortho}}$ and $\mathbf{Q}^{\mathrm{Tetra}}$ modes can be tuned to agree with experiment by accessing additional $e$-$e$ Jahn-Teller activity otherwise unavailable.

## IV. CONCLUSION

An isotropic Hubbard correction, such as the $U_{\mathrm{eff}}$ methodology, is unable to simultaneously reproduce the band gap, experimental level of Jahn-Teller distortion and magnetic ordering of bulk LaMnO$_3$. At small $U_{\mathrm{eff}}$, A-AFM magnetic ordering is correctly stabilized but the gap and structural distortions are underestimated. With increasing $U_{\mathrm{eff}}$ values, the gap and crystal structure are reproduced but FM ordering is incorrectly stabilized. The $U|J$ approach, with its explicit exchange dependence on orbital symmetry, provides a better picture of electronic, magnetic and structural properties of LaMnO$_3$. The origin of the $U|J$ success is the Hund's coupling accounted for by the spatial/orbital dependence of the dedicated exchange terms that depend on $J$. These terms selectively polarize orbital occupation through highly anisotropic energy splitting in the Mn $d$ manifold. Only the addition of $J$ terms, rather than crystal field or direct Coulomb $U$, can provide appropriate and large enough anisotropic splitting within the $t_{2g}$ and $e_g$ manifolds. Orbital order due to the short range $J$ makes possible the combination of long-range FM exchange in the (010) plane, and AFM exchange between {010} planes, to stabilize the A-AFM ordered ground state. Soft phonon modes ($e$-$l$ Jahn-Teller) and electronic occupation polarization ($e$-$e$ Jahn-Teller) contribute jointly to the insulating state, with the latter predominant. The experimental Jahn-Teller distortion magnitude can only be achieved by adding the anisotropy $J$ provides on top of the direct Coulomb occupancy polarization. The best description of LaMnO$_3$ is achieved within the PBEsol+$U$ framework when $U = 8$ eV and $J = 1.9$ eV.
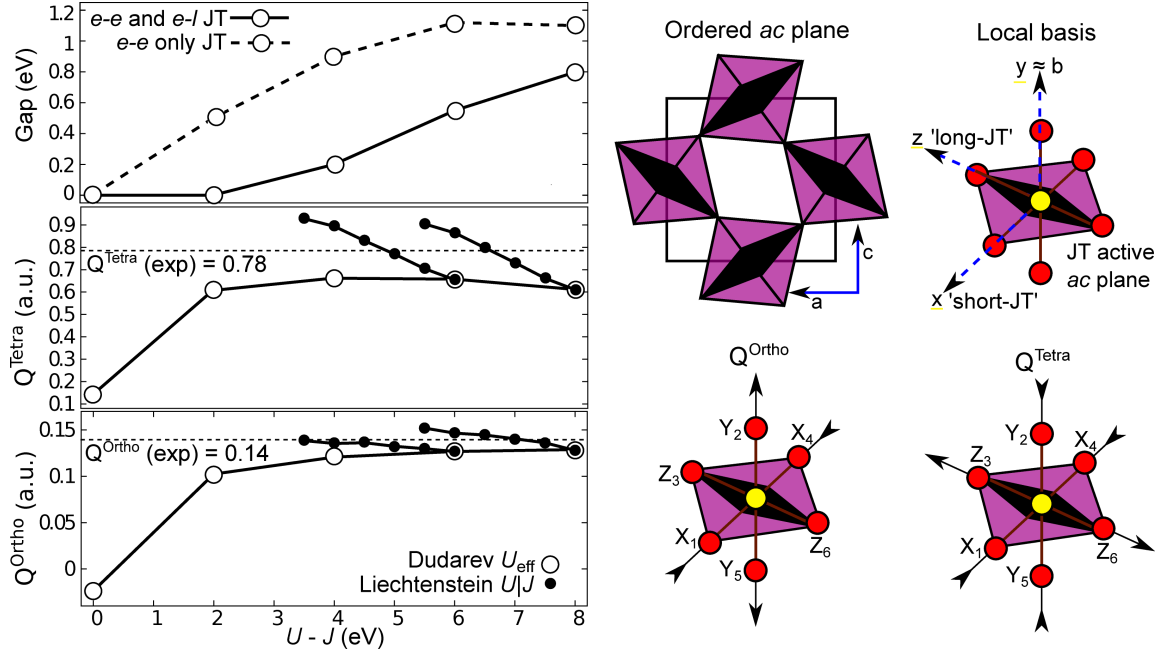
Figure 8: *Left top panel:* Band gap of LaMnO$_3$ versus $U - J$ within the $U_{\text{eff}}$ approach for fully relaxed structures where both electron-lattice and electron-electron interactions are active (dashed line, *e-l* and *e-e*) and for structures with the Jahn-Teller distortion frozen out so only electron-electron interactions are active (solid line, *e-e* only). *Left bottom and middle panels:* Jahn-Teller normal modes versus $U - J$ within the $U_{\text{eff}}$ approach (white circles), and within the $U|J$ approach (black circles) for $U$ fixed to 8 eV and 6 eV with $J$ varied. *Right panels:* Orbitally ordered and strongly Jahn-Teller active *ac* plane, the local basis convention, and $\mathbf{Q}^{\text{Ortho}}$ and $\mathbf{Q}^{\text{Tetra}}$ modes.

## V. REFERENCES

[1] C. Franchini, R. Ková čik, M. Marsman, S. Murthy, J. He, C. Ederer and G. Kresse, *Journal of Physics: Condensed Matter*, 2012, **24**, 235602.

[2] I. Solovyev, N. Hamada and K. Terakura, *Physical review letters*, 1996, **76**, 4825–4828.

[3] L. Feiner and A. Oleś, *Physical Review B*, 1999, **59**, 3295–3298.

[4] A. Millis, *Physical Review B*, 1997, **55**, 6405–6408.

[5] A. Millis, *Nature*, 1998, **392**, 147–150.

[6] M. Baldini, V. Struzhkin, A. Goncharov, P. Postorino and W. Mao, *Physical Review Letters*, 2011, **106**, 066402.

[7] I. Loa, P. Adler, A. Grzechnik, K. Syassen, U. Schwarz, M. Hanfland, G. Rozenberg, P. Gorodetsky and M. Pasternak, *Physical Review Letters*, 2001, **87**, 125501.

[8] Y. Tokura, *Science*, 2000, **288**, 462–468.

[9] M. Uehara, S. Mori, C. Chen and S. Cheong, *Nature*, 1999, **399**, 560–563.

[10] Q. Chu, X. Wang, B. Li, F. Liu and X. Liu, *RSC Advances*, 2013, **3**, 21311.

[11] Y. Joly, J. Lorenzo and S. Grenier, *Nature*, 2003, **430**, 7–8.

[12] Y. Tokura, *Reports on Progress in Physics*, 2006, **69**, 797–851.

[13] H. Chen and S. Ismail-Beigi, *Physical Review B*, 2012, **86**, 024433.

[14] J. He and C. Franchini, *Physical Review B*, 2012, **3**, 32.

[15] G. Rao, J. Sun, K. Bärner and N. Hamad, *Journal of Physics: Condensed Matter*, 1999, **11**, 1523–1528.

[16] N. Mathur, G. Burnell, S. Isaac and T. Jackson, *Nature*, 1997, **246**, 170–170.

[17] R. Mahendiran, S. Tiwary, A. Raychaudhuri, R. Mahesh and C. Rao, *Physical review. B, Condensed matter*, 1996, **54**, R9604–R9607.

[18] J. Garcia-Barriocanal, J. Cezar, F. Bruno, P. Thakur, N. Brookes, C. Utfeld, A. Rivera-Calzada, S. Giblin, J. Taylor, J. Duffy, S. Dugdale, T. Nakamura, K. Kodama, C. Leon, S. Okamoto and J. Santamaria, *Nature communications*, 2010, **1**, 82.

[19] H. Chen, Q. Qiao, M. Marshall, A. Georgescu, A. Gulec, P. Phillips, R. Klie, F. Walker, C. Ahn and S. Ismail-Beigi, *Nano letters*, 2014, **14**, 4965–4970.

[20] D. Muñoz, N. Harrison and F. Illas, *Physical Review B*, 2004, **69**, 085115.

[21] S. Dudarev, G. Botton, S. Savrasov, C. Humphreys and A. Sutton, *Physical Review B*, 1998, **57**, 1505–1509.

[22] A. Liechtenstein, V. Anisimov and J. Zaanen, *Physical Review B*, 1995, **52**, R5467–R5471.

[23] H. Sawada, Y. Morikawa, K. Terakura and N. Hamada, *Physical Review B*, 1997, **56**, 12154–12160.

[24] T. Hashimoto, S. Ishibashi and K. Terakura, *Physical Review B*, 2010, **82**, 045124.

25 M. Wu, E. Benckiser, M. Haverkort, A. Frano, Y. Lu, U. Nwankwo, S. Bruck, P. Audehm, E. Goering, S. Macke, V. Hinkov, P. Wochner, G. Christiani, S. Heinze, G. Logvenov, H. Habermeier and B. Keimer, *Physical Review B*, 2013, **88**, 125124.

26 G. Kresse and J. Furthmüller, *Computational Materials Science*, 1996, **6**, 15–50.

27 G. Kresse and J. Furthmüller, *Physical Review B*, 1996, **54**, 11169–11186.

28 J. Perdew and A. Zunger, *Physical Review B*, 1981, **23**, 5048–5079.

29 J. Perdew, A. Ruzsinszky, G. Csonka, O. Vydrov, G. Scuseria, L. Constantin, X. Zhou and K. Burke, *Physical Review Letters*, 2008, **100**, 136406.

30 J. Perdew, K. Burke and M. Ernzerhof, *Physical Review Letters*, 1996, **77**, 3865–3868.

31 P. Blöchl, *Physical Review B*, 1994, **50**, 17953–17979.

32 G. Kresse and D. Joubert, *Physical Review B*, 1999, **59**, 11–19.

33 V. Anisimov and Y. Izyumov, *Electronic structure of strongly correlated materials*, Springer, 2010, vol. 163.

34 V. Anisimov, F. Aryasetiawan and A. Liechtenstein, *Journal of Physics: Condens. Matter*, 1997, **9**, 767–808.

35 B. Himmetoglu, A. Floris, S. de Gironcoli and M. Cococcioni, *International Journal of quantum Chemistry*, 2014, **114**, 14–49.

36 H. Nakamura, N. Hayashi, N. Nakai, M. Okumura and M. Machida, *Physica C: Superconductivity*, 2009, **469**, 908–911.

37 T. Jeong and W. Pickett, *Journal of Physics: Condensed Matter*, 2006, **18**, 10529.

38 E. Bousquet and N. Spaldin, *Physical Review B - Condensed Matter and Materials Physics*, 2010, **82**, 1–4.

39 D. Tompsett, D. Middlemiss and M. Islam, *Physical Review B*, 2012, **86**, 205126.

40 B. Himmetoglu, R. Wentzcovitch and M. Cococcioni, *Physical Review B*, 2011, **84**, 1–8.

41 T. Mellan, K. Maenetja, P. Ngoepe, S. Woodley, C. Catlow and R. Grau-Crespo, *Journal of Materials Chemistry A*, 2013, **1**, 14879.

42 E. Cockayne and L. Li, *Chemical Physics Letters*, 2012, **544**, 53–58.

43 N. Kovaleva, A. Boris, C. Bernhard, A. Kulakov, A. Pimenov, A. Balbashov, G. Khaliullin and B. Keimer, *Physical Review Letters*, 2004, **93**, 147204.

44 N. Sakai, H. Fjellvag and B. Lebech, *Acta Chemica Scandinavica*, 1997, **51**, 904–909.

45 T. Arima, Y. Tokura and J. Torrance, *Physical Review B*, 1993, **48**, 17006–17009.

46 T. Saitoh, A. Bocquet, T. Mizokawa, H. Namatame, A. Fujimori, M. Abbate, Y. Takeda and M. Takano, *Physical Review B*, 1995, **51**, 13942–13951.

47 J. Jung, K. Kim, D. Eom, T. Noh, E. Choi, Y. Jaejun, Y. Kwon and Y. Chung, *Physical Review B*, 1997, **55**, 04823.

48 R. Krüger, B. Schulz, S. Naler, R. Rauer, D. Budelmann, J. Bäckström, K. Kim, S. Cheong, V. Perebeinos and M. Rübhausen, *Physical Review Letters*, 2004, **92**, 097203–4.

49 J. Lee, K. Delaney, E. Bousquet, N. Spaldin and K. Rabe, *Physical Review B - Condensed Matter and Materials Physics*, 2013, **88**, 1–8.

50 G. Trimarchi and N. Binggeli, *Physical Review B*, 2005, **71**, 035101–9.

51 J. Elemans, *Journal of Solid State Chemistry*, 1971, **242**, 238–242.

52 Y. Nohara, A. Yamasaki, S. Kobayashi and T. Fujiwara, *Physical Review B*, 2006, **1**, 1–5.

53 A. Georges, L. Medici and J. Mravlje, *Annual Review of Condensed Matter Physics*, 2013, **4**, 137–178.

54 F. Lu, D.-M. Chen and L.-J. Zou, *Chinese Physics Letters*, 2009, **26**, 097501–5.

55 K. Kugel and D. Khomski, *Soviet Physics Uspekhi*, 1982, **25**, 231–256.

56 J. Goodenough, *Journal of Physics and Chemistry of Solids*, 1958, **6**, 287–297.

57 J. Kanamori, *Journal of Physics and Chemistry of Solids*, 1959, **10**, 87–98.

58 M. Nicastro and C. Patterson, *Physical Review B*, 2002, **65**, 205111–15.

59 H. Meskine, H. König and S. Satpathy, *Physical Review B*, 2001, **64**, 1–13.

60 J. Rodríguez-Carvajal, M. Hennion, F. Moussa, A. Moudden, L. Pinsard and A. Revcolevschi, *Physical Review B*, 1998, **57**, R3189–R3192.

61 J. Jung, K. Kim, T. Noh, E. Choi and J. Yu, *Physical Review B*, 1998, **57**, 43–46.

62 F. Moussa, M. Hennion, J. Rodriguez-Carvajal, H. Moudden, L. Pinsard and a. Revcolevschi, *Physical Review B*, 1996, **54**, 15149–15155.

63 J. H. van Vleck, *Journal of Chemical Physics*, 1939, **220**, 72–84.

64 J. Kanamori, *Journal of Applied Physics*, 1960, **31**, S14.

65 D. Khomski, *Transition metal compounds*, 2014, vol. 2, p. 485.

66 D. Khomski, *Physica Scripta*, 2005, **72**, 8–14.

67 W. Yin, D. Volja and W. Ku, *Physical Review Letters*, 2006, **96**, 116405–4.

## Acknowledgments

## Appendix A: DFT+$U$ expressions

We begin with the $U|J$ rotationally invariant DFT+$U$ total energy expression[22] written for a single atomic site (since the corrections are linear sums over atomic sites),

$$E_{\mathrm{DFT}+U|J} = E_{\mathrm{DFT}} + E_U - E_{\mathrm{dc}}\ .$$

$E_{\mathrm{DFT}}$ is the total DFT energy using some flavor of exchange and correlation, the Coulombic +$U$ correction energy is

$$E_U = \frac{1}{2} \sum_{\sigma,\sigma',m^i} (m\sigma m''\sigma'|V|m'\sigma m'''\sigma') \times$$
$$(\rho^\sigma_{m'm}\rho^{\sigma'}_{m'''m''} - \rho^\sigma_{m'''m}\rho^\sigma_{m'm''}\delta_{\sigma\sigma'})$$

and the double-counting correction $E_{\mathrm{dc}}$ is

$$E_{\mathrm{dc}} = \sum_\sigma \frac{(U-J)}{2} N_\sigma(N_\sigma - 1) + \frac{U}{2} N_\sigma N_{\bar\sigma}\ .$$

In the above expressions, $V(\mathbf{r},\mathbf{r}') = 1/|\mathbf{r}-\mathbf{r}'|$ is the bare Coulomb interaction, $\sigma$ labels spin where $\bar\sigma$ is the opposite spin to $\sigma$, $m$ labels angular momentum states of the atomic shell under consideration ($d$ orbitals for Mn in this paper), $\rho^\sigma_{mm'}$ is the single-particle density matrix, $N_\sigma = trace(\rho^\sigma) = \sum_{m,m'} \rho^\sigma_{mm'}\delta_{mm'}$ is the number of electrons on the site of spin $\sigma$, and $U$ and $J$ are the direct and exchange Coulomb parameters.

The matrix elements of $V$ are defined by $(m\sigma m''\sigma'|V|m'\sigma m'''\sigma') = \int dr \int dr'\ \phi^*_{m\sigma}(\mathbf{r})\phi_{m'\sigma}(\mathbf{r}) \frac{1}{|\mathbf{r}-\mathbf{r}'|} \phi^*_{m''\sigma'}(\mathbf{r}')\phi_{m'''\sigma'}(\mathbf{r}')$. The matrix elements of $V$ are further decomposed for an atomic shell with angular momentum $l$ via

$$(m\sigma m''\sigma'|V|m'\sigma m'''\sigma') =$$
$$\delta_{m-m',m'''-m''} \sum_{k=0}^{2l} c^k(lm,lm')c^k(lm''',lm'')F^k$$

where $c^k$ and $F^k$ are standard atomic Slater angular integrals and radial integrals. For $d$ shells, $U = F^0$, $J = (F^2 + F^4)/14$ and $F^4/F^2 = 0.625$ are the canonical choices[22]. Thus only two parameters are needed to specify the radial integrals: $F^0 = U$, $F^2 = (112/13)J$ and $F^4 = (70/13)J$.

To make progress with expressions for $E_U$ and $E_{\mathrm{dc}}$ which are given in terms of $\rho^\sigma_{mm'}$ and $N_\sigma$, we need rewrite these expressions in terms of the occupancy eigenvalues of the density matrix, $f_{i\sigma}$. Denoting the eigenvectors of $\rho^\sigma_{mm'}$ as $V^\sigma_{m,i}$ so that

$$\rho^\sigma_{mm'} = \sum_i V^\sigma_{m,i}\ f_{i\sigma}\ \left(V^\sigma_{m',i}\right)^*$$

we may insert this expansion into the expression for $E_U$. After some algebraic manipulations, using the fact that $c^0(lm,lm') = \delta_{mm'}$ for the $k=0$ term and the unitarity of the eigenvector $V^\sigma$ matrices, we find

$$E_U = \frac{U}{2}\left(N^2 - \sum_{i\sigma} f^2_{i\sigma}\right) +$$
$$\frac{1}{2}\sum_{\sigma,\sigma',i,j} C^{\sigma\sigma'}_{ij} f_{i\sigma}f_{j\sigma'} - X^\sigma_{ij} f_{i\sigma}f_{j\sigma}\delta_{\sigma\sigma'}$$

where $N = \sum_\sigma N_\sigma$ is the total electron count on the site, and the Coulombic $C^{\sigma\sigma'}$ and exchange $X^\sigma$ correction matrices are given by

$$C^{\sigma\sigma'}_{ij} = \sum_{k=2}^{2l} F^k \sum_{mm'm''m'''} \delta_{m-m',m'''-m''} \times$$
$$(V^\sigma)^\dagger_{im} c^k(lm,lm') V^\sigma_{m'i} (V^{\sigma'})^\dagger_{jm'''} c^k(lm''',lm'') V^{\sigma'}_{m''j}$$

and

$$X^\sigma_{ij} = \sum_{k=2}^{2l} F^k \sum_{mm'm''m'''} \delta_{m-m',m'''-m''} \times$$
$$(V^\sigma)^\dagger_{im} c^k(lm,lm') V^\sigma_{m'j}\ (V^\sigma)^\dagger_{im'''} c^k(lm''',lm'') V^\sigma_{m''j}\ .$$

The Coulomb correction $C^{\sigma\sigma'}$ matrices have zero average over all entries, a fact easily shown by using some basic properties of the Slater angular integrals. The same can be done for the exchange correction matrices by separating out a constant term

$$X^\sigma_{ij} = \Delta X^\sigma_{ij} + J(1 - \delta_{ij})\ .$$

Substituting this into the previous $E_U$ expression and subtracting the double-counting term $E_{\mathrm{dc}}$ to cancel common terms then yields the total energy

$$E_{\mathrm{DFT}+U|J} = E_{\mathrm{DFT}} + \frac{U-J}{2}\sum_{i\sigma}(f_{i\sigma} - f^2_{i\sigma}) +$$
$$\frac{1}{2}\sum_{\sigma,\sigma',i,j} C^{\sigma\sigma'}_{ij} f_{i\sigma}f_{j\sigma'} - \Delta X^\sigma_{ij} f_{i\sigma}f_{j\sigma}\delta_{\sigma\sigma'}$$

which is in the form of the DFT+$U_{\mathrm{eff}}$ (Dudarev) energy[21] plus a correction involving the $C^{\sigma\sigma'}$ and $\Delta X^\sigma$ matrices and the occupancies. Therefore, the $U|J$ scheme can be viewed as a correction to the $U_{\mathrm{eff}}$ method which includes additional Coulombic and exchange terms stemming from exchange integrals between different orbitals: this is because both $C^{\sigma\sigma'}$ and $\Delta X^\sigma$ are proportional to $J$ and thus the orbital shape dependence of the Coulombic interactions on the site, something neglected by the $U_{\mathrm{eff}}$ scheme.

The correction to the eigenvalue follows from the occupancy derivative of the added terms to the DFT energy

$$\frac{\partial(E_U - E_{\mathrm{dc}})}{\partial f_{i\sigma}} = (U - J)\left(\frac{1}{2} - f_{i\sigma}\right) +$$
$$\sum_{j\sigma'} \mathrm{C}_{ij}^{\sigma\sigma'} f_{j\sigma'} - \Delta\mathrm{X}_{ij}^{\sigma} f_{j\sigma}\delta_{\sigma\sigma'}.$$

In what follows, it is more convenient to work with vectors and matrices. Thus if we collect all occupancies $f_{i\sigma}$ into a column vector $f_\sigma$, then the above eigenvalue correction can be more compactly written as

$$\nabla_{f_\sigma}(E_U - E_{\mathrm{dc}}) = (U - J)\left(\frac{1}{2} - f_\sigma\right) +$$
$$J\left[\mathrm{A}^\sigma f_\sigma + \mathrm{B}^\sigma f_{\bar\sigma}\right]$$

where we have peeled off the constant $J$ and also indicated same spin and opposite spin occupancy dependences *via* the unitless matrices

$$\mathrm{A}^\sigma = (\mathrm{C}^{\sigma\sigma} - \Delta\mathrm{X}^\sigma)/J$$

and

$$\mathrm{B}^\sigma = \mathrm{C}^{\sigma\bar\sigma}/J.$$

We now proceed to actual example cases to compute numerical values for the $\mathrm{A}^\sigma$ and $\mathrm{B}^\sigma$ matrices. The simplest assumption is to take the spherical harmonic states $Y_{lm}$ as the eigenbasis of the density matrix $\rho^\sigma$. This means $\mathrm{V}^\sigma = \mathrm{I}$ and one can directly compute the matrices using numerical values for Slater angular integrals. The results are

$$\mathrm{A}^\sigma = \begin{pmatrix}
 & Y_{22} & Y_{21} & Y_{20} & Y_{2,-1} & Y_{2,-2} \\
\hline
Y_{22} & 0 & -0.52 & -0.52 & 0.17 & 0.86 \\
Y_{21} & -0.52 & 0 & 0.52 & -0.17 & 0.17 \\
Y_{20} & -0.52 & 0.52 & 0 & 0.52 & -0.52 \\
Y_{2,-1} & 0.17 & -0.17 & 0.52 & 0 & -0.52 \\
Y_{2,-2} & 0.86 & 0.17 & -0.52 & -0.52 & 0
\end{pmatrix}$$

and

$$\mathrm{B}^\sigma = \begin{pmatrix}
 & Y_{22} & Y_{21} & Y_{20} & Y_{2,-1} & Y_{2,-2} \\
\hline
Y_{22} & 0.72 & -0.40 & -0.63 & -0.40 & 0.72 \\
Y_{21} & -0.40 & 0.37 & 0.06 & 0.37 & -0.40 \\
Y_{20} & -0.63 & 0.06 & 1.14 & 0.06 & -0.63 \\
Y_{2,-1} & -0.40 & 0.37 & 0.06 & 0.37 & -0.40 \\
Y_{2,-2} & 0.72 & -0.40 & -0.63 & -0.40 & 0.72
\end{pmatrix}.$$

However, this basis is not the most relevant for solid state systems such as perovskite oxides. For high symmetry situations, the eigenbasis of the density matrix will be given by $t_{2\mathrm{g}}$ $(xy, yz, xz)$ and $e_{\mathrm{g}}$ $(3z^2 - r^2, x^2 - y^2)$ states. The conversion matrix is

$$\mathrm{V}^\sigma = \begin{pmatrix}
0 & 1/\sqrt{2} & i/\sqrt{2} & 0 & 0 \\
0 & 0 & 0 & -i/\sqrt{2} & 1/\sqrt{2} \\
1 & 0 & 0 & 0 & 0 \\
0 & 0 & 0 & i/\sqrt{2} & 1/\sqrt{2} \\
0 & 1/\sqrt{2} & -i/\sqrt{2} & 0 & 0
\end{pmatrix}$$

if we choose the order $(3z^2 - r^2, x^2 - y^2, xy, yz, xz)$. The transformed matrices are now in the more useful basis with entries

$$\mathrm{A}^\sigma = \begin{pmatrix}
 & 3z^2-r^2 & x^2-y^2 & xy & yz & xz \\
\hline
3z^2-r^2 & 0 & -0.517 & -0.517 & 0.517 & 0.517 \\
x^2-y^2 & -0.517 & 0 & 0.861 & -0.172 & -0.172 \\
xy & -0.517 & 0.861 & 0 & -0.172 & -0.172 \\
yz & 0.517 & -0.172 & -0.172 & 0 & -0.172 \\
xz & 0.517 & -0.172 & -0.172 & -0.172 & 0
\end{pmatrix},$$

and

$$\mathrm{B}^\sigma = \begin{pmatrix}
 & 3z^2-r^2 & x^2-y^2 & xy & yz & xz \\
\hline
3z^2-r^2 & 1.143 & -0.630 & -0.630 & 0.059 & 0.059 \\
x^2-y^2 & -0.630 & 1.143 & 0.288 & -0.401 & -0.401 \\
xy & -0.630 & 0.288 & 1.143 & -0.401 & -0.401 \\
yz & 0.059 & -0.401 & -0.401 & 1.143 & -0.401 \\
xz & 0.059 & -0.401 & -0.401 & -0.401 & 1.143
\end{pmatrix}.$$

These matrices directly tell us how the $U|J$ scheme corrects the energy eigenvalues beyond the $U_{\mathrm{eff}}$ energy shift. For example, the diagonal entries of $\mathrm{B}^\sigma$ indicate that occupying any orbital pushes up the energy of the opposite spin orbitals by $1.14J$.

As another example, if we have an ion such as $\mathrm{Mn}^{4+}$ with a full up spin and empty down spin $t_{2\mathrm{g}}$ shell, so that $f_\uparrow = (0, 0, 1, 1, 1)$ and $f_\downarrow = 0$, then for the up spin orbitals the energy correction beyond $U_{\mathrm{eff}}$ is $(0.52, 0.52, -0.34, -0.34, -0.34)J$ which destabilizes the same spin $e_{\mathrm{g}}$ and stabilizes the same spin $t_{2\mathrm{g}}$ while for spin down orbitals the situation is exactly reversed with energy correction $(-0.52, -0.52, 0.34, 0.34, 0.34)J$. A final example is a full $t_{2\mathrm{g}}^6$ shell such as $\mathrm{Co}^{3+}$ which gives zero correction to the $U_{\mathrm{eff}}$ scheme. The above two matrices form the basis for various analyses in the main text.

## Appendix B: Density matrix rotation to local axis representation

In typical DFT+$U$ approaches, the electronic structure is given in terms of density matrices for each subspace, *e.g.*, the $d$ shell. Unfortunately the orthogonal global axial representation which is most efficacious for computation is often not most convenient for analysis and understanding. This happens in calculations with non-trivial unit cells where inequivalent oxygen octahedra surround transition metal ions. Octahedral rotations and tilts mean the global axial system for the calculation, here labelled $x', y', z'$, will differ from the native local axes, labelled $x, y, z$. Native axes for each octahedron point along the transition metal-O bonds, and form the natural basis for understanding the electronic structure of the transition metal $d$ orbitals. We describe the

details of a simple approach that rotates the density matrix, from the global to the local basis *via* polynomial transformations, with LaMnO$_3$ as our example.

We choose a particular Mn ion and its nearest neighbor O atoms which identify an octahedral cage. Three Mn-O bonds are chosen that point in approximately orthogonal directions. The bonds are indexed $i = 1, 2, 3$, and we compute the difference vectors from the Mn to O positions: $\mathbf{u}_i = \mathbf{r}(O_i) - \mathbf{r}(Mn)$. These vectors are then normalized and define the local axes for the Mn. We create a $3 \times 3$ rotation matrix R connecting the global $x', y', z'$ and local $x, y, z$ systems

$$\begin{pmatrix} x' \\ y' \\ z' \end{pmatrix} = \mathrm{R} \begin{pmatrix} x \\ y \\ z \end{pmatrix} = \begin{pmatrix} R_{11} & R_{12} & R_{13} \\ R_{21} & R_{22} & R_{23} \\ R_{31} & R_{32} & R_{33} \end{pmatrix} \begin{pmatrix} x \\ y \\ z \end{pmatrix}$$

defined by placing the unit vectors $\mathbf{u_i}$ in the columns of R. It is at this point that we choose the ordering of the unit vectors to reflect the physical questions at hand. Note, a traditional choice is to align $z$ with the apical bond, but

other choices are possible: for example, in our work we have placed $y$ along the non-Jahn-Teller 'apical' Mn-O (see Figure 4) while $x$ and $z$ span the Jahn-Teller active plane.

This rotation represents a linear polynomial transformation relating $x', y', z'$ to $x, y, z$. The angular behavior of each $d$ orbital is quadratic in the coordinates: $3z'^2 - r'^2$, $x'^2 - y'^2$, $x'y'$, $y'z'$, $x'z'$, so it is straightforward to plug in and algebraically transform the polynomials to the unprimed (local) coordinate system. Performing the substitutions, using the orthogonal nature of the R matrix, and collecting terms, we find

$$\begin{pmatrix} 3z^2 - r^2 \\ x^2 - y^2 \\ xy \\ yz \\ xz \end{pmatrix} = \mathrm{C} \begin{pmatrix} 3z'^2 - r'^2 \\ x'^2 - y'^2 \\ x'y' \\ y'z' \\ x'z' \end{pmatrix}$$

where the matrix C is

$$\mathrm{C} = \begin{pmatrix} \frac{1}{2}(3R_{33}^2 - 1) & \frac{1}{2}(R_{13}^2 - R_{23}^2) & \frac{1}{2}R_{13}R_{23} & \frac{1}{2}R_{23}R_{33} & \frac{1}{2}R_{13}R_{33} \\ \frac{3}{2}(R_{31}^2 - R_{32}^2) & \frac{1}{2}(R_{11}^2 - R_{12}^2 + R_{22}^2 - R_{21}^2) & \frac{1}{2}(R_{11}R_{21} - R_{12}R_{22}) & \frac{1}{2}(R_{21}R_{31} - R_{22}R_{32}) & \frac{1}{2}(R_{11}R_{31} - R_{12}R_{32}) \\ 6R_{31}R_{32} & 2(R_{11}R_{12} - R_{21}R_{22}) & R_{11}R_{22} + R_{12}R_{21} & R_{21}R_{32} + R_{22}R_{31} & R_{11}R_{32} + R_{12}R_{31} \\ 6R_{32}R_{33} & 2(R_{12}R_{13} - R_{22}R_{23}) & R_{12}R_{23} + R_{13}R_{22} & R_{22}R_{33} + R_{23}R_{32} & R_{12}R_{33} + R_{13}R_{32} \\ 6R_{31}R_{33} & 2(R_{11}R_{13} - R_{21}R_{23}) & R_{11}R_{23} + R_{13}R_{21} & R_{21}R_{33} + R_{23}R_{31} & R_{11}R_{33} + R_{13}R_{31} \end{pmatrix}.$$

The matrix C is not unitary due to the fact that the bare polynomials $3z'^2 - r'^2, x'^2 - y'^2, x'y', y'z', x'z'$ are orthogonal but are not normalized. The normalization is done by averaging the squares of the functions $(3z'^2 - r'^2)/r'^2, (x'^2 - y'^2)/r'^2, x'y'/r'^2, y'z'/r'^2, x'z'/r'^2$ over the surface of the unit sphere. We place these averages, which are $4/5, 4/15, 1/15, 1/15, 1/15$, respectively, on the diagonals of a diagonal scaling matrix S and then form the scaled and unitary transformation matrix $\mathrm{D} = \mathrm{S}^{1/2} \, \mathrm{C} \, \mathrm{S}^{-1/2}$ which is our final matrix relating the $d$ orbitals in primed and unprimed coordinates.

To give a feeling for how the method works, we take the experimental structure for LaMnO$_3$ crystal with $a = 5.736$ Å, $b = 7.703$ Å and $c = 5.540$ Å, as in Figure 1. In experimental structured LMO, consider the octahedron about the Mn atom at $(0.00, 0.00, 2.77)$ Å, which has two basal oxygens at $O^1 = (1.12, -0.31, 1.26)$ Å and $O^2 = (1.75, 0.31, 4.03)$ Å, and an apical oxygen at $O^3 = (-0.07, 1.93, 2.37)$ Å. We form the normalized $\mathbf{u}_i$ vectors, compute R and then C and upon normalization find

$$\mathrm{D} = \begin{pmatrix} 0.06 & 0.04 & 0.01 & 0.23 & 0.31 \\ -0.03 & 0.16 & 0.88 & -0.24 & 0.64 \\ 0.58 & -0.74 & 0.97 & -0.09 & 0.27 \\ 0.78 & 0.54 & -0.71 & -0.19 & -0.33 \\ -0.05 & -0.20 & -2.76 & -0.29 & 0.99 \end{pmatrix}.$$

D can now be used to diagonalize the $5 \times 5$ density matrix in the sub-space of the Mn $d$ orbitals. For a DFT+$U|J$ calculation with $U = 8$ eV and $J = 2$ eV, fixed at the experimental structure, the Mn $d$ eigensystem is

$$\phi_\sigma = \begin{pmatrix} f_{i\sigma} & 0.42 & 0.96 & 0.97 & 0.98 & 0.99 \\ \hline 3z'^2 - r'^2 & 0.50 & 0.12 & 0.80 & -0.22 & -0.19 \\ x'^2 - y'^2 & 0.54 & 0.17 & -0.53 & -0.07 & -0.63 \\ x'y' & -0.10 & 0.80 & -0.02 & -0.56 & -0.21 \\ y'z' & 0.28 & -0.57 & 0.09 & 0.77 & -0.07 \\ x'z' & -0.60 & 0.11 & 0.25 & 0.21 & -0.72 \end{pmatrix}.$$

Here each eigenvector is a column vector with its eigenvalue $f_{i\sigma}$ provided above it. Before rotation, it is hard to easily read off the nature of each eigenstate by inspection. After rotation, the eigenvectors in the local basis are given by

$$
\mathrm{D}\phi_\sigma = \begin{pmatrix}
\begin{array}{c|ccccc}
f_{i\sigma} & 0.42 & 0.96 & 0.97 & 0.98 & 0.99 \\
\hline
3z^2 - r^2 & -0.17 & -0.05 & -0.07 & 0.13 & -0.97 \\
x^2 - y^2 & 0.99 & 0.05 & -0.07 & 0.03 & -0.17 \\
xy & 0.00 & -0.01 & 0.05 & -0.99 & -0.15 \\
yz & -0.03 & -0.99 & -0.09 & 0.00 & 0.07 \\
xz & 0.01 & +0.11 & -0.99 & -0.06 & 0.07
\end{array}
\end{pmatrix} .
$$

The local basis eigenvectors are clearly much "purer" as each vector has a component whose magnitude is 0.97 or larger. And thus each configuration is easy to read off by inspection: the partially occupied state in the first column is essentially the $x^2 - y^2$ state while the last column shows that the $3z^2 - r^2$ has become filled. We have strong orbital polarization in the $e_\mathrm{g}$ manifold. This indicates the rotation to local octahedral coordinates successfully diagonalized the eigensystem, and that the local basis is physically relevant for understanding the electronic structure.